UCRL-ID-129096-98

High-Power Laser Source Evaluation

C. A. Back, C. D. Decker, J. F. Davis, S. Dixit, J. Grun, R. A. Managan,
F. J. D. Serduke, G. F. Simonson, L. J. Suter, C. R. Wuest, F. Ze

July 1998

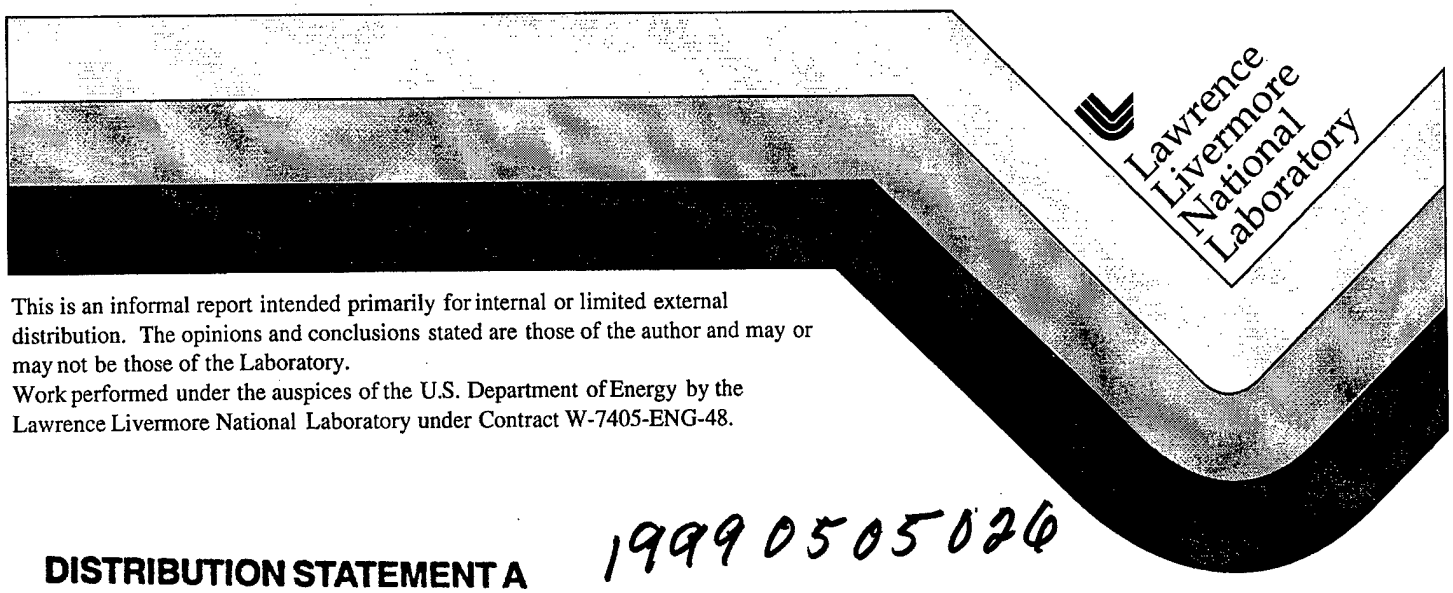

Work performed under the auspices of the U.S. Department of Energy by the Lawrence Livermore National Laboratory under Contract W-7405-ENG-48.

Lawrence Livermore National Laboratory
Livermore, California 94550

High-Power Laser Source Evaluation

Christina A. Back, Christopher D. Decker, John F. Davis*, Sham Dixit, Jacob Grun†, Robert A. Managan, Franklin J. D. Serduke, Gregory F. Simonson, Laurance J. Suter, Craig R. Wuest, and Fred Ze

July 1998

Final Report on IACROs 97-3022 and 97-3048
to
Mr. Richard Gullickson
Dr. Ralph Schneider

Defense Special Weapons Agency

***Alme and Associates**
†Naval Research Laboratory

for more information, please contact
Franklin Serduke
LLNL L-183
Livermore, CA 94550
1(925)422-6592

TABLE OF CONTENTS

I-Introduction and Overview

Robust Nuclear-Weapons-Effects Testing (NWET) capability will be needed for the foreseeable future to ensure the performance and reliability, in nuclear environments, of the evolving U.S. stockpile of weapons and other assets. Ongoing research on the use of high-energy lasers to generate environments of utility in nuclear weapon radiation effects simulations is addressed in the work described in this report. Laser-driven hohlraums and a variety of other targets have been considered in an effort to develop NWET capability of the highest possible fidelity in above-ground experiments. The envelope of large-system test needs is shown as the gray region in fig. 1. It does not represent the spectrum of any device; it is just the envelope of the spectral region of outputs from a number of possible devices. It is a goal of our laser-only and ignition-capsule source development work to generate x rays that fall somewhere in this envelope. One of the earlier appearances of this envelope is in ref. 1.

The Defense Special Weapons Agency provided important support for the work described herein. A total of $520K was provided in the 1997 IACROs 97-3022 for Source Development and 97-3048 for Facilitization. The period of performance specified in the Statement of Work ran from 28 February 1997 until 30 November 1997. This period was extended, by agreement with DSWA, for two reasons: 1) despite the stated period of

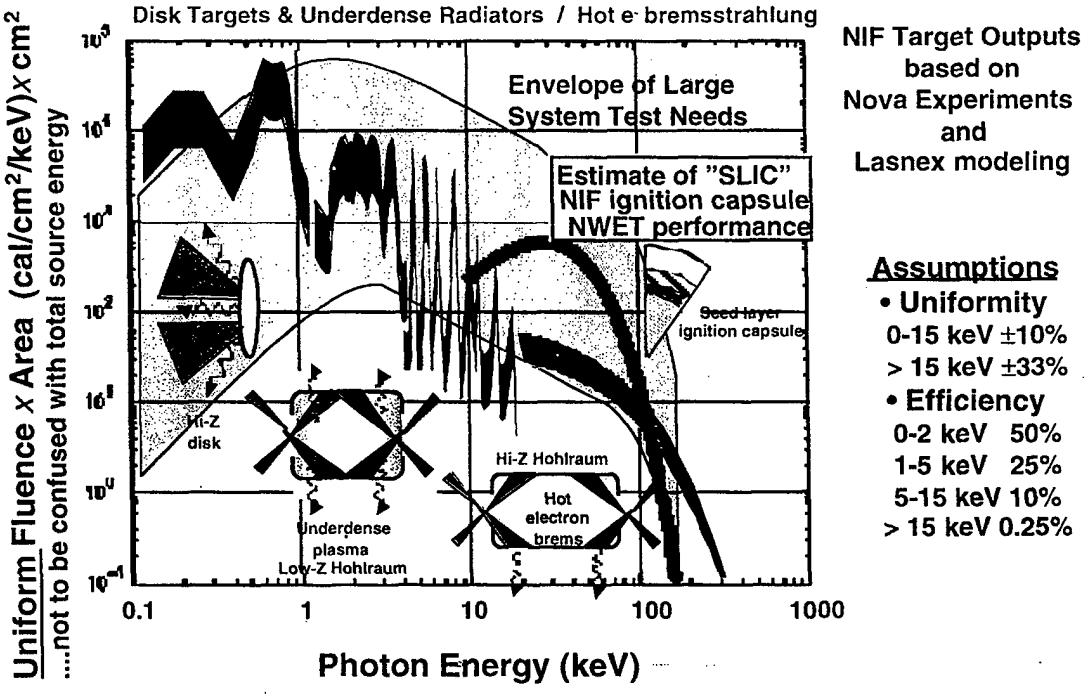

Figure 1: Plot of the uniform fluence-area products of various NIF non-ignition sources plus an estimate of the performance of the Seed-Layer Ignition Capsule against a background of the envelope of large-system test requirements suggested by Dr. Cyrus P. Knowles of Jaycor.

performance, funds were not available at LLNL to begin this work until somewhat later in the fiscal year, and 2) we agreed to stretch the current resources until follow-on funds were in hand, to minimize effects of ramping down and up again.

The tasks addressed in this report are the following:

1) Non-ignition-source model benchmarking and design. This involves analysis of existing and new data on laser-only sources to benchmark LASNEX predictions
2) Non-ignition-source development experiments
3) Ignition capsule design to improve total x-ray output and simplify target fabrication
4) Facilitization of source arrays and of the NIF for NWET

A funding triad that includes the Defense Special Weapons Agency, the NIF Project and LLNL's Defense Technology Department supports the work that is reported in this document. The additional work presented here shows how the DSWA-funded work integrates with the larger effort.

There has been continued success in the development and fielding of the potentially longer-duration non-ignition beryllium-can sources. There have been advances in understanding of the relevant physics of these underdense radiators as well as further experimental support for the validity of the predictions. This report includes results on our SLIC designs (Seed Layer Ignition Capsules) that permit optimism for prospects of improving the hot-x-ray-to-neutron ratio and total hot x-ray yield for NIF ignition targets.

An important summary of the laser-only x-ray environments appears again in this year's document. This summary serves as an audit trail for the non-ignition-sources that are projected for NIF based on experimental results and on projections of LASNEX modeling.

Reference:

1. NWET Applications for NIF Workshop (a compendium of viewgraphs) 15-17 March 1994. ed. by Gregory Simonson of LLNL

II-Experimental Measurements of X-Ray Emission from Xenon-filled Beryllium Hohlraums

II-1. Introduction:

As a follow-on to experiments in 1996, three xenon-gas-filled beryllium hohlraum shots were performed in July 1997. These shots were on hohlraums that were redesigned based on post-shot calculations of the previous targets (see next article). The targets were improved by using larger laser entrance holes (LEHs) to eliminate refraction of the laser beam that was caused by low density Be plasma that formed at the inside edges of the LEHs. A small percentage of krypton (Z=36) gas was added to the xenon (Z=54) to attempt a measurement of the plasma temperature using ratios of various x-ray lines from helium-like krypton. Target diagnostics showed uniform heating of a 2 mm long gas-filled can and an x-ray pulse that was longer in duration. The peak of the x-ray emission and x-ray pulse duration are more consistent with the predictions from simulations. The conversion efficiency measured by the absolutely-calibrated spectrometer was similar to previous determinations, approximately 12 % for the 2 mm diameter hohlraums.

II-2. Experimental Setup:

As before, experiments were performed using the NOVA laser. Due to newly lowered Nova beam energy constraints, we used approximately 32 kJ of 0.35 μm laser light in 2 ns flat-topped intensity profile. The 1996 shots had about 40 kJ available. This operational energy limit was lowered due to damage to laser optics. The laser beams entered through the holes in the endcaps of the target and irradiated the inside of a Be cylinder that was filled with xenon gas and a 10%-20% admixture of krypton for temperature diagnostics. The lasers heat the gas to form a highly ionized plasma that emits x-rays. These x-rays pass through the walls of the Be cylinder and are detected by both time-resolved and time-integrated diagnostics. The physical target dimensions were similar to previous shots - 1.8 mm outer length (1.6 mm inner length) and 2 mm in diameter; however, in this design the laser entrance holes (LEHs) were 1.5 mm in diameter instead of 1.0 mm. Detailed post-shot calculations of the 1.0 mm LEHs of the target indicated that the x-ray pulse and heating were negatively affected by refraction of the laser beams by a low density Be plasma that formed at the edges of the entrance holes. For the current experiments, the LEHs were increased from 1 mm to 1.5 mm in diameter to eliminate the problem and to test this aspect of the calculations. Furthermore, one Be hohlraum was increased to 3.6 mm in diameter to test a scaling of the conversion efficiency with size of the target. The gas fill in the targets was slightly modified from the previous targets in that Xe was doped with 10% or 20% Kr to enable measurements of temperature by K-shell spectroscopy of the almost-fully-ionized krypton. In all other target fabrication respects, *i.e.*, glue, pressure tests, Be wall thickness, etc., the targets were similar to the previous series of experiments.

The diagnostic complement was enhanced by the addition of more x-ray diodes and x-ray film packs. Previously-used diagnostics were fielded again and included absolutely-calibrated x-ray crystal spectrometers called Henways, x-ray streak cameras, and x-ray imagers. New diagnostics were x-ray diodes that gave an independent second measurement of the conversion efficiency and x-ray film packs which measured the angular symmetry of the x-ray emission.

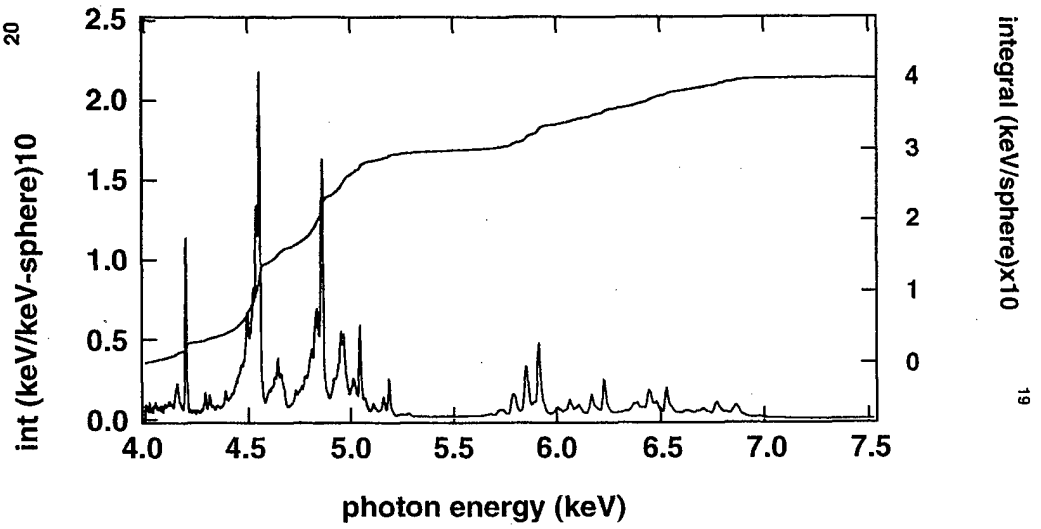

Figure 1. Spectrum from a time-integrated x-ray spectrometer. This target was a filled to 1 atm with 80% Xe and 20% Kr. It was 1.8 mm in length and 2.0 mm in diameter. The ordinates of this plot are uncertain due to difficulties with the absolute calibration of the instrumentation. The left axis shows the x-ray intensity. The right axis shows the cumulative integral of this x-ray intensity.

II-3. Experimental Results

Three shots were performed in this series of experiments in 1997. All were on 1 atm targets. One was filled with 80% Xe and 20% Kr and two were filled with 90% Xe and 10% Kr. These Xe-filled hohlraum targets were irradiated by the Nova laser to investigate the x-ray output of laser-heated targets in the photon energy range of 4 to 10 keV. Two targets with a 2 mm diameter were fielded - one with 80% Xe and 20 % Kr, and the other with 90 % Xe and 10 % Kr. The third target was 3.6 mm in diameter with a 90% Xe and 10 % Kr gas fill. The Nova laser delivered 32 kJ of laser energy in a 2 ns flat-topped laser pulse that supersonically ionizes the Xe gas. Target shot numbers were 27072309, 27072311, and 27072403 (large can).

Conversion efficiency was measured by both the Henway crystal spectrometers as before, and with x-ray diodes brought from NRL. In fig. 1 is an example of the spectrum and its running integral from shot 27072309. The running integral is plotted on the right-hand axis. The n= 3-2 transitions are found in the 4-to-5 keV range and the n=4-2 and 5-2 transitions are in the 5.5-to-7 keV range. For each shot, these data are collected for two positions, one from the side and the other along the axis of the hohlraum. The x-ray output from these small hohlraums were not angularly dependent, in contrast to previous shots with smaller laser entrance holes. The large hohlraum, however, did show a slight asymmetry. The two shots performed on the 2 mm diameter (small) hohlraums gave a conversion efficiency of 15% into the 4 to 7.5 keV photon energy range. The larger hohlraums were less efficient and gave a conversion efficiency of 9.4% from the side and 13.0% along the laser axis. This larger hohlraum was filled to the same pressure and therefore density, however, they were less efficient which is consistent with x-ray images of the hohlraum that showed that the entire volume of gas was not uniformly heated.

Measurements by the x-ray diodes tend to give a lower conversion efficiency, near 7%. However, the analysis of these data was hampered by a low signal-to-noise ratio, which makes the error bar large. While this conversion efficiency is still much larger than ablative disk targets in this regime, the difference between the two conversion efficiency measurements by the Henway Bragg crystal spectrometers and the x-ray diodes fielded on the same shot is under investigation. Both of these measurements depend on the absolute calibration of the diagnostics. In the case of the spectrometer, the reflectivity of the crystal is the largest error, and this can easily account for a 50 % error bar. For the diodes, this depends on the calibration of the anodes on a source of measured flux.

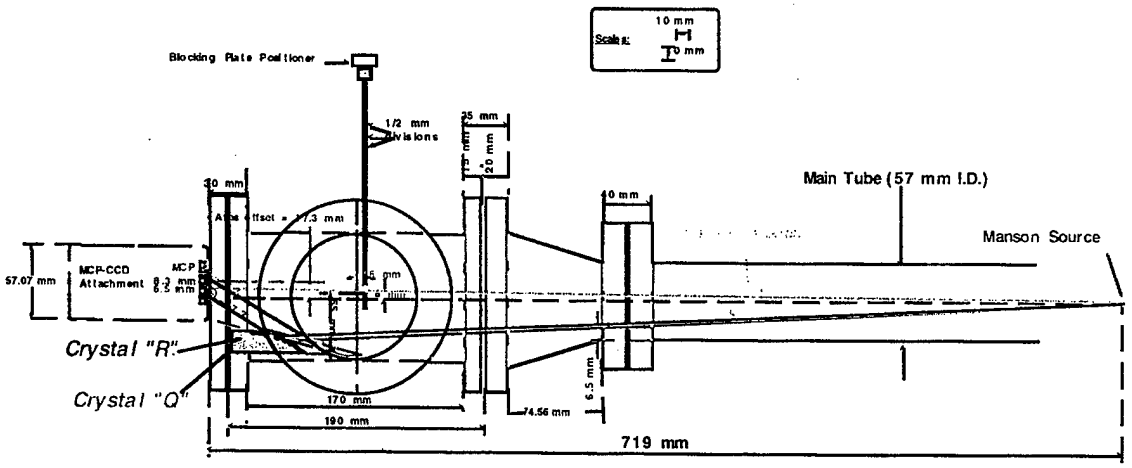

Figure 2a. Schematic of experimental setup designed by Fred Ze to measure integrated reflectivity of the curved Henway crystals used in the experiments. A Manson source and microchannel plate were used to record the data

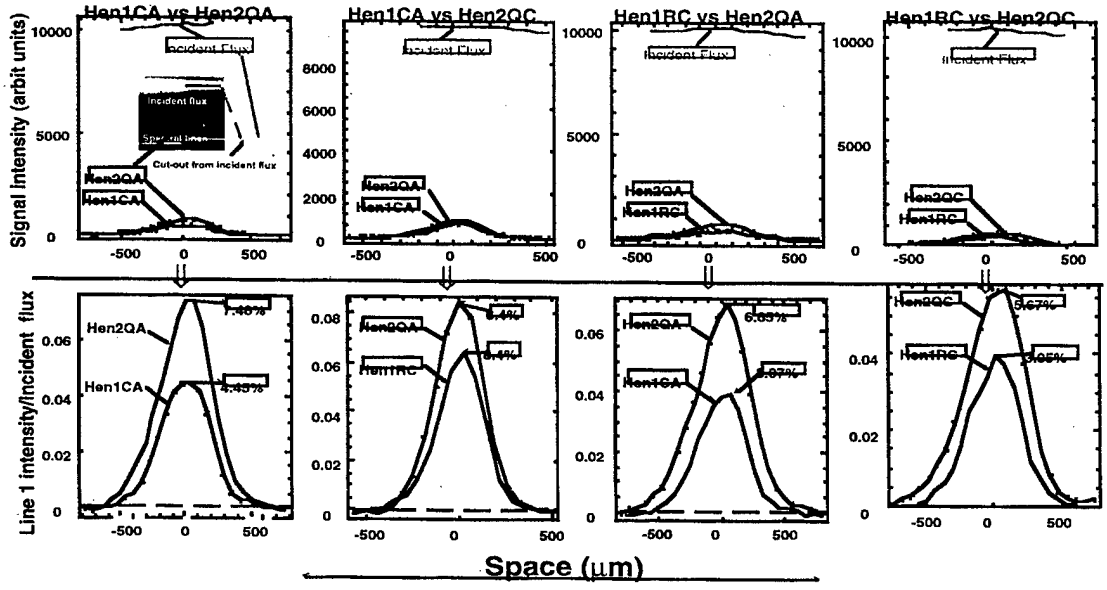

Figure 2b. Measurement of the integrated reflectivity of a curved Henway crystal used in the experiments. The top curve indicates the incident x-rays source intensity, the bottom curve is a measure of the reflectivity corrected for the microchannel plate response.

For the crystals, we have performed measurements on a stationary-anode source in the laboratory. This does not measure the rocking curve of the crystal, however, it does measure the integrated reflectivity. Figure 2 shows some results from supplementary measurements on a laboratory Manson x-ray source that we are continuing to analyze.

The angular dependence was examined by the use of x-ray film packs that were located at two different points within the chamber. They were passive diagnostics that were attached to diagnostic-insertion SIM carts that were driven into the chamber for the gated and streaked diagnostics. These film packs were filtered for both above 4 keV photon energies, and also for above 13 keV photon energies and were time integrated. The results showed a less-than 5 % asymmetry.

The temporal dependence of the Xe emission ($h\nu$ = 4-7 keV) was only obtained on the large hohlraum. In the first two shots, time-dependent data were not obtained due to diagnostic difficulties. The large hohlraum shows marked improvement in conversion efficiency compared to the targets shot in 1996 due to the improved design of the hohlraum. Figure 3 shows the temporal history of the emission compared to the data from the 1996 series. The red curve is from the 1997 data while the blue and green curves are from the 1996 data. In the 1997 data, the emission lasts for nearly the full 2 ns duration of the laser pulse whereas before, the refraction of the beam at the laser entrance holes caused a reduced emission after 1 ns.

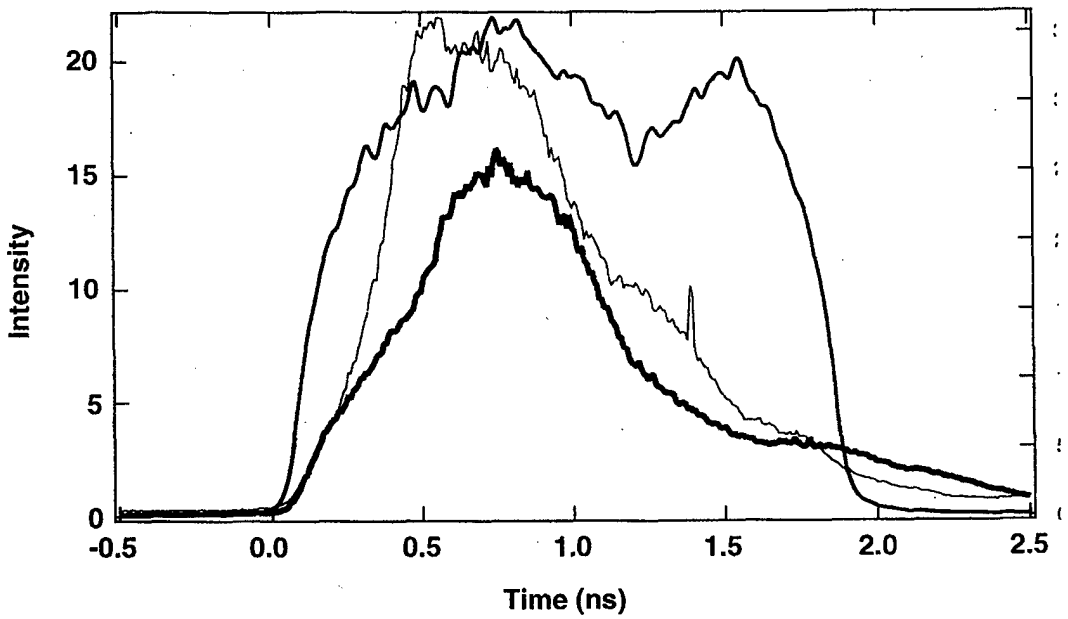

Figure 3. Temporal history of the x-ray pulse of the L-shell of Xe. The red curve is the large-can new data showing a longer duration of the x-rays of interest. The green curve is for the old design 1996 target with a smaller LEH and a 1 atm fill and the blue curve is for the 1996 target with a 2 atm fill.

Imaging results showed a vast improvement in the uniformity of the heated target. They are recorded on a gated pinhole imager and filtered for appropriate photon energy ranges. For the smaller 2 mm diameter targets, the x-ray emission is fairly uniform in the side-on images. This is in contrast to the previous target design (experiments in 1996) that showed a central cold region, even late in time. Figure 4 shows x-ray images of the target from the side view filtered for two different photon energy bands. The lasers enter the hohlraum

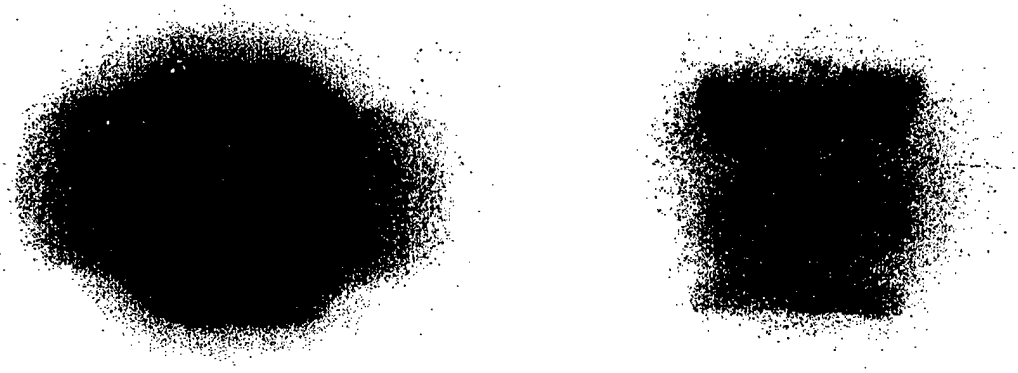

Xe image @ 1.3 ns ($h\nu > 4$ keV) Kr image @ 1.3 ns ($h\nu > 13$ keV)

Figure 4. Two-dimensional x-ray images of the target. The image of the left is for photon energies > 4 keV and is dominated by the Xe emission at 1.3 ns . The image on the right is filtered for photon energies > 13 keV; At 1.3 ns these come primarily from Kr in the target.

from the left and right of the target. On the left is an image filtered for x-rays at 4 keV and above. Here it is fairly uniform in the second half of the pulse and some plasma is seen escaping the laser entrance holes. On the right is an x-ray images filtered for $h\nu > 13$ keV. A two lobed emission pattern is still visible early in time, but at about 1.5 ns, it remains non-uniform even later in the pulse. The data show that the lasers have already propagated into the center of the hohlraum by 1 ns for Xe ($h\nu$>4 keV images) and by 1.3 ns in the Kr ($h\nu$>13 keV images). This x-ray emission is strongly weighted by the density and we are presently comparing these images with computer simulations of the target.

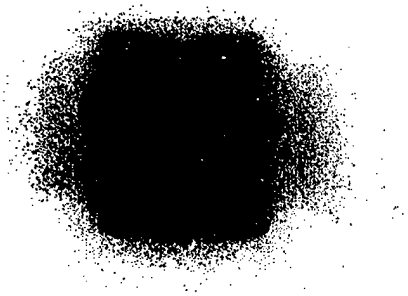

Xe image @ 1.8 ns ($h\nu > 4$ keV)

Figure 5. X-ray image for a 1 atm pressure target at photon energies $h\nu > 4$ keV. The entire inner volume 2 mm in diameter and 1.8 mm long is recorded in emission at a time 1.8 ns after the laser starts.

A variation in Xe emission over this region at a later time, ~ 1.8 ns, was measured to be ~10 % on shot 27072311 and this has a high correlation with the laser energy on target. In the case shown below in figure 5, the energy of the laser beams irradiating the top of the target was slightly lower. In the future, beam balance can be requested to avoid this non-uniformity.

The larger targets still show small volumes of gas that are not heated enough to emit >4 keV x-rays. Figure 6 gives an example of these images to compare to those in figure 3, but for the larger target. We currently comparing these images with calculations of the emission.

Images taken end-on from the axial pinhole imager are shown for the small and large hohlraum in figure 7. The blue and red circles show the diameter of the two different sized cans viewed end-on. The smaller

Large hohlraum Xe image (>4 keV)@ 1.8 ns Kr image (>13 keV)@ 1.8 ns

Figure 6. X-ray image for a 1 atm pressure target at photon energies hv > 4 keV at 1.8 ns into the pulse for a 3.6 mm diameter target. In the Xe image, the larger volume is not uniform and the corners of the target are not heated sufficiently to emit > 4 keV x-rays. In the Kr image, the emission is in the center and does not spread to the full diameter of the can.

diameter target images show bright emission at the wall of the 2 mm diameter can which corresponds to the positions of the incoming beams on the inside wall of the hohlraum.

The brighter emission at the wall is of considerable interest since the wall is made of Be and should not emit more than the gas fill at these photon energies. The Be wall material is provided by Brush Wellman and the material certification shows that this material consists

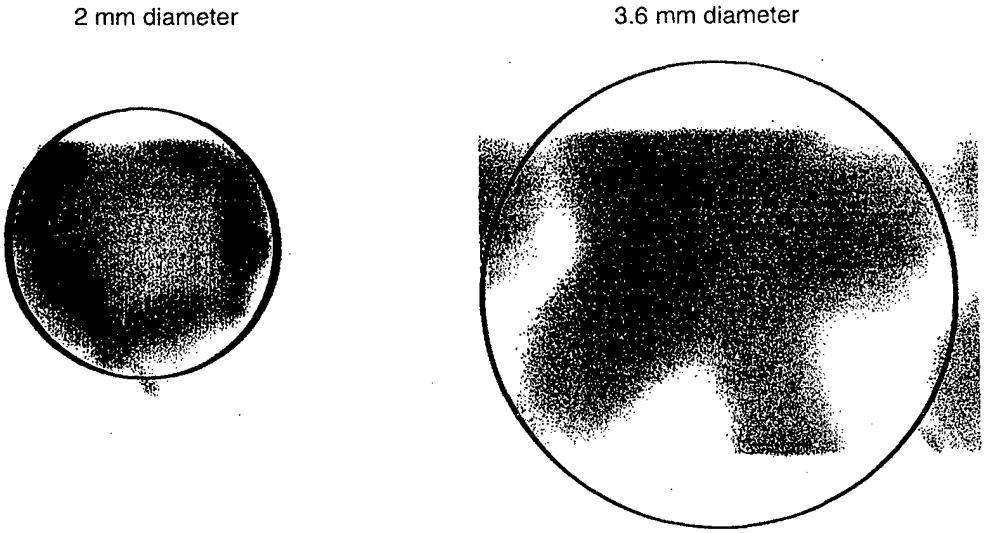

Figure 7. X-ray images from gated axial pinhole cameras filtered for x-rays > 4keV at about 1 ns into the experiment. . The left image is from a 2 mm diameter hohlraum and the right image is from the 3.6 mm larger diameter hohlraum.

of 99.39 % Be. (P.O. # 1448403), where the contaminants are largely low to mid-Z materials. The highest Z contaminant is Ti at 0.004 % which is a small enough percentage to have a negligible effect on the emission, even if Ti He α lines at 4.7 keV are produced. Independent target characterization on site at LLNL of the actual target shows impurities of O, Al, Si, S, Cl, K, Ca and Fe in small quantities that total less than 0.1 % by weight. Again this confirms that the impurities are insufficient to cause significant amounts of emission in these target images. Thus, the higher emission observed is probably an effect due to the higher density of the gas near at the wall since the Be is expected to ablate towards the center of the hohlraum and compress the Xe plasma.

In the 3.6 mm diameter hohlraum this compression effect is not visible and instead "columns" of heated gas are produced where the laser beam passes. The intensity of the emission in these images is not the same as those in the side-on view because of different gains in the x-ray framing cameras.

During these experiments, there was also an attempt to measure the krypton K-shell lines that can serve as a temperature diagnostic. The geometry is shown below in figure 8. The

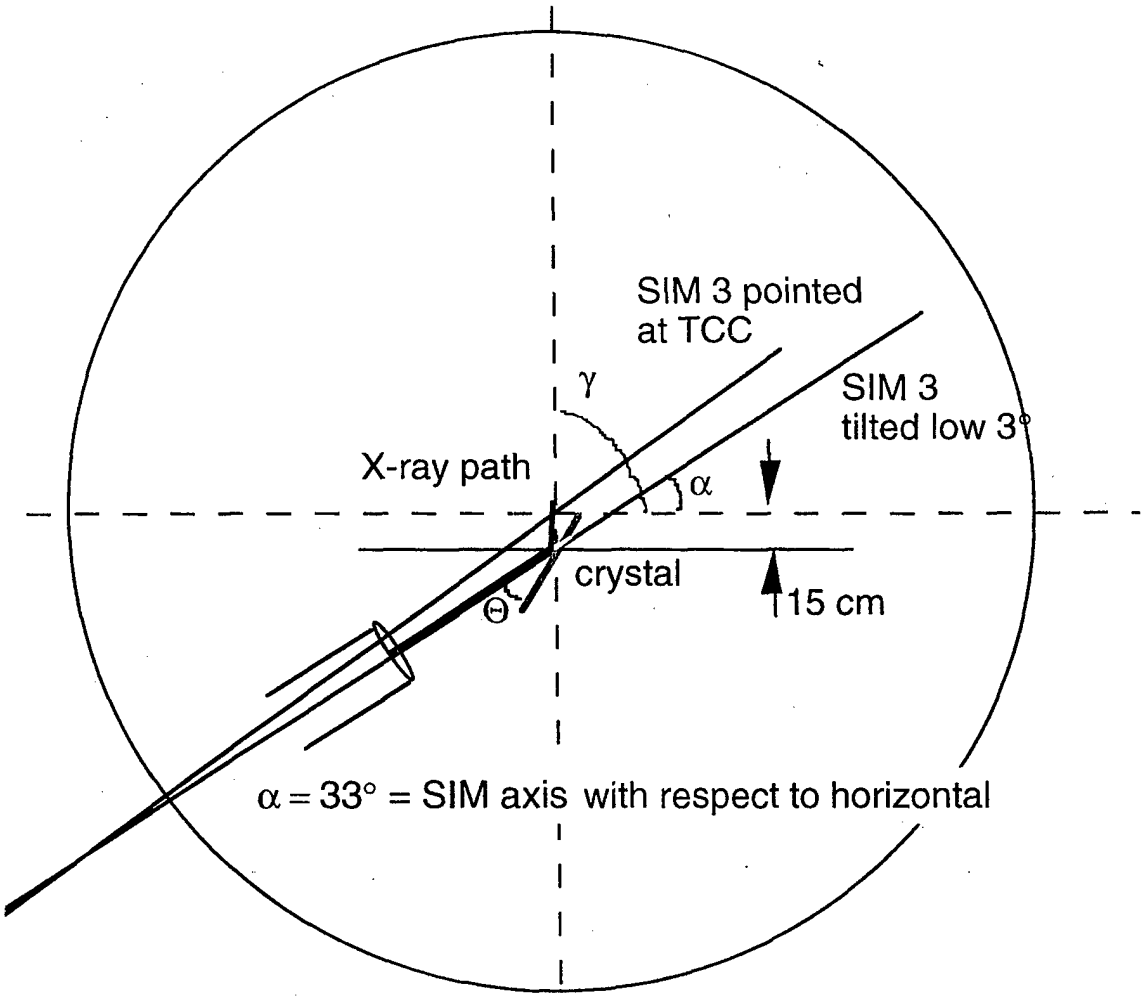

Figure 8. Schematic of the target chamber showing the SIM tube geometry fielded for the temperature sensitive diagnostic. The outside circle represents the 2.2 meter radius Nova target chamber. The blue line is the line of sight of the SIM tube tilted low by 3 ° and the red line shows the x-ray path. The light blue line is the position of the crystal.

diagnostic was an x-ray streak camera coupled to a Bragg crystal. The krypton He-α line is at 13.1 keV; high-resolution spectroscopy at this photon energy has not been done before at Nova. We need to get high resolution in order to use the ratio of the Li-like satellite lines to the He-α line as a temperature diagnostic. As this ratio becomes larger, the temperature is lower because more Li-like satellite lines exist at lower temperatures.

Experimentally two different crystals were fielded. The sensitivity to these high energy x-rays is not well measured because they are not commonly used and stationary x-ray calibration sources have difficulty achieving these photon energies. In figure 8, the outside circle is a schematic of the 2.2 meter radius target vacuum chamber and the SIM tube is explicitly shown coming up from the bottom left. Due to the Bragg angle needed for sufficient resolution, the spectrometer was pointed below target chamber center to accommodate a quartz (5052) or a LiF (422) Bragg crystal; these have a 2d spacing of 1.624 and 1.652 Å respectively. Ge (111) was considered but not used because of possible fluorescence of the Ge itself at these energies. Alignment of the diagnostic was tested on a maintenance day at Nova and offsets for the SIM tube were calibrated at that time.

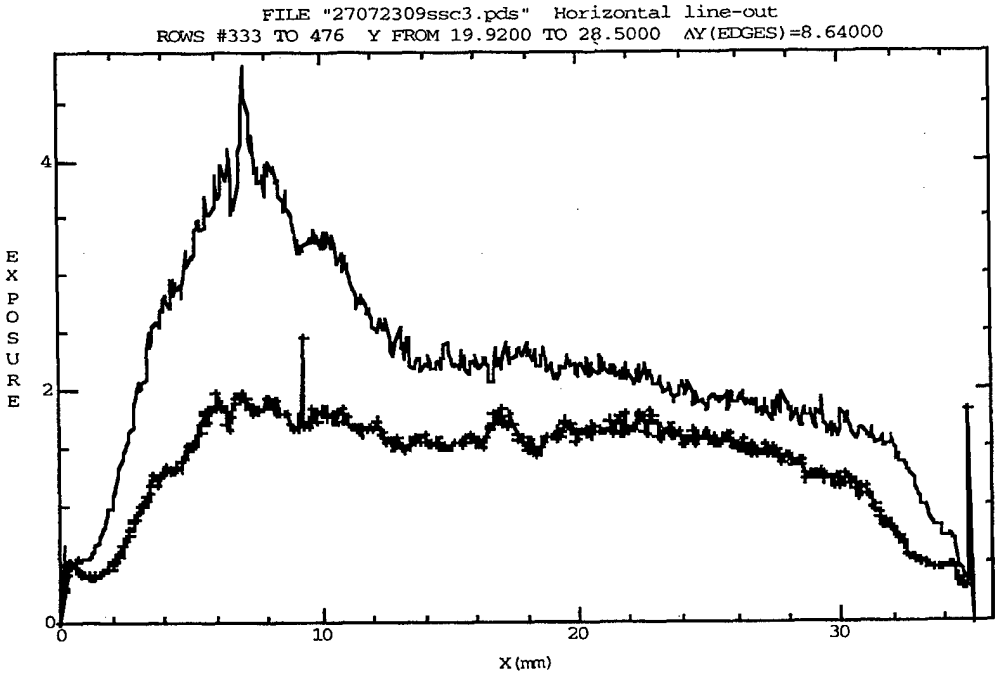

Figure 9. Spectrum from two different shots, taken at 1.5 ns. The peak at x = 7 mm is due to krypton He-α emission at 13.1 keV

An example of the data obtained on this instrument is shown in figure 9. A streaked x-ray spectrometer shows a pronounced double bump in time in the Xe/Kr continuum emission with the Kr He-α line appearing in the second half of the 2 ns pulse on the first target. Below are a preliminary spectral lineouts showing the data from two different shots. The peak is due to emission from the He-α line located on the abscissa at approximately x=7 mm is at 13.1 keV. The emission is weaker than expected and therefore the determination of temperature from this data is difficult due to low signal-to-noise ratio.

II-4. Conclusions

Experimental measurements have been performed on laser-produced plasmas that show they can generate a significant quantity of x-rays above 4 keV. In summary, these targets show that the design of the hohlraums is much improved from the previous experiments. This improvement is principally due to the larger laser entrance hole size, which eliminates refraction of the incoming laser beams. We are continuing to analyze the data. The results show a conversion efficiency similar to the 1996 targets, but a much more uniform heating of the target. The large-scale computer simulations for conversion efficiency and duration of the x-ray pulse better model these data. For a Xe filled hohlraum volume of 5 mm^3, we are able to produce a 7-13 % efficient underdense radiator. The larger hohlraums are both predicted and measured to have about 25% lower x-ray conversion efficiency. There are three-dimensional features in the data that should be studied in further modeling.

Side-on imaging of the targets indicates we successfully produced targets with the entire length of the hohlraum to be in emission. The uniformity was measured to be ~10 % that can be entirely attributed to beam balance and this can be improved with better balance of the beam energies in future targets.

End-on imaging of the small cans that shows higher-intensity radiation near the walls under the laser spots suggests that there may be a tamping of the emitting gas by blowoff of the beryllium hohlraum material. By contrast, the large hohlraum emission appeared to be along the laser beams and did not achieve early or mid-time higher-intensity radiation near the walls. However the sideways extent of the columns of radiation seen in the large hohlraums could give clues of electron conductivity in these plasmas.

New filter pack diagnostics and corrections to the original data based on the relative calibrations have reduced the apparent asymmetry of the previous data to within uncertainties of the measurements.

Outstanding issues include the x-ray crystal and diode calibrations to reduce the error bar and inconsistencies in the conversion efficiency numbers. The conversion efficiency ranged from 5% to 20%, depending on the angle of view.

First attempts at a K-shell krypton temperature diagnostic were encouraging but inconclusive. These photon energies (> 13 keV) have not been measured on Nova laser-produced plasmas before and the small number of shots makes diagnostic development difficult. The krypton He-α line was observed, but the signal level is quite low. Two-dimensional images of the targets show the region of emission for Kr ($h\nu$>13 keV) is smaller than for Xe ($h\nu$>4 keV). This diagnostic is still being developed.

III-Lasnex Modeling of Underdense Plasma Radiators

III-1. Introduction

Underdense plasma radiators have been studied as part of a program to produce multi-keV x-ray sources for use on large lasers such as NIF. The initial work in this area focussed on xenon-filled gas bags that were driven by the Nova laser. More recently, it has been proposed to use laser-heated Xe-filled Be hohlraums or cans; these sources are predicted to have a high conversion efficiency and an x-ray output duration longer than those from laser-heated gas bags. As a result, experiments were executed to assess the performance of these underdense radiators and to test our ability to model them.

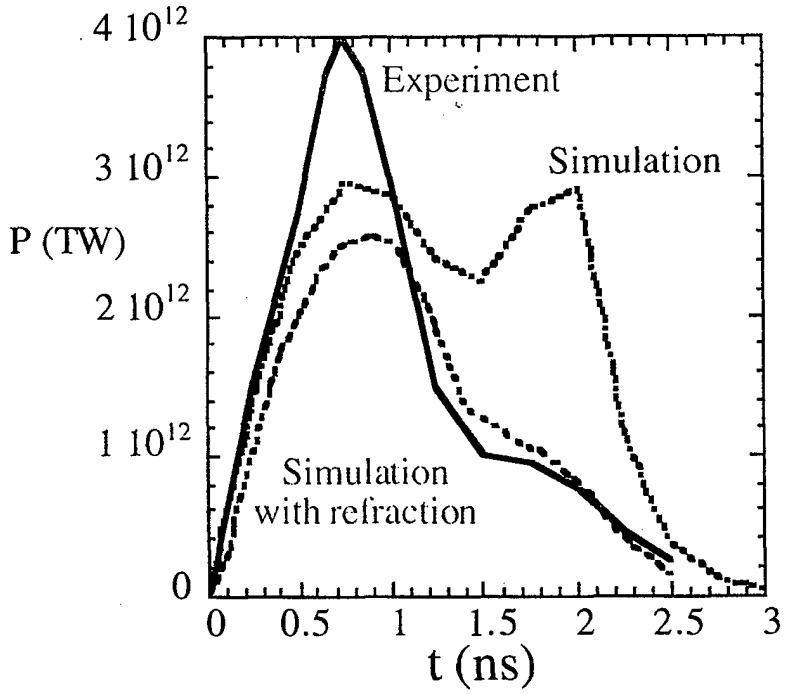

Figure 1. Comparison of the 1996 underdense plasma temporal emission profile with two simulations: one with refraction of the incoming laser beams, the other without. It is very suggestive that refraction was truncating the x-ray emission and is the basis for the increased laser-entrance hole diameter in the 1997 shots described in the previous article.

III-2. Discussion

In this report we present simulations that were performed after the first set of gas-filled-can experiments. These simulations help to understand the differences between modeling and the experimental results as well as to aid in designing the next round of experiments. Simulations and experiment were not in full accord following the first round of beryllium-can experiments. The duration of the emission lasted only about 1 ns in contrast to the

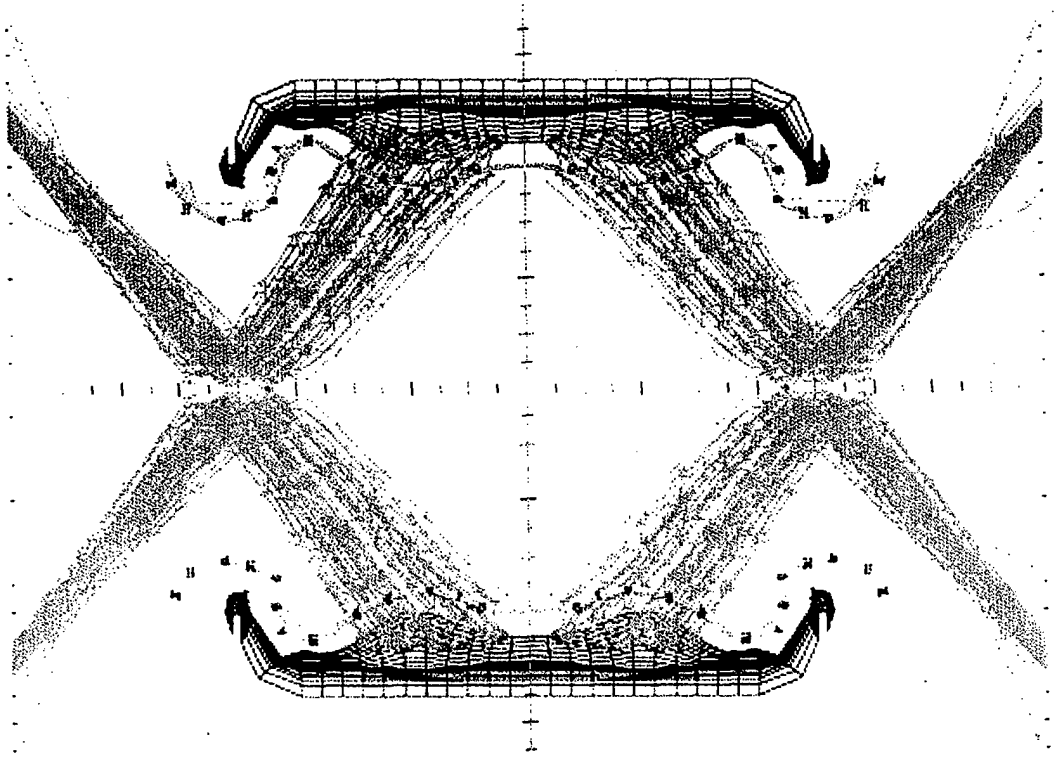

Figure 2. Lasnex modeling of the large-(1.5 mm diameter) laser-entrance-hole beryllium hohlraum that is filled with 1 atmosphere of xenon gas. In practice, only one quadrant of this picture is modeled because of symmetry. The laser beams are shown in magenta, the Be hohlraum in black and the interface between the beryllium blowoff and the xenon gas is shown in cyan. This shows that the larger LEH has solved the late-time beam refraction problem. Tick marks are separated by 100 μm.

predicted 2 ns. The experimental images also showed spatial gaps in the emission patterns, whereas simulations indicated that the emission should not show a gap at the center. A series of simulations was performed which attempted to mock up effects such as inhibited electron transport, beam deflection and backscattering. None of these effects appeared to recover the experimental results.

However, the experimental emission images indicated that large amounts of plasma had escaped the can through the laser entrance hole (LEH). In the first set of Lasnex simulations, material outside the Be can was lost from the calculation during rezones. After modifying our zoning scheme to follow the escaping plasma properly, we found that Be blow-off from the lip of the laser entrance hole was impinging into the path of the laser beam. This near critical density plasma was found to refract the laser beam so severely that the beam would no longer enter into the can. With refraction included we found that the temporal history of the x-ray emission agreed well with experiments. To show this we plot in figure 1 the experimental results (red) along with the initial simulations (blue) and the new simulations (green) including refraction.

As a result of the simulations which included Be blow-off, modifications to the Be can design were made which alleviated the refraction problem. In particular, the laser entrance hole diameter was increased from 1.0 mm to 1.5 mm. The dimensions of the new design are shown in figure 2 where we plot the can zoning (black) , the laser rays (magenta), and

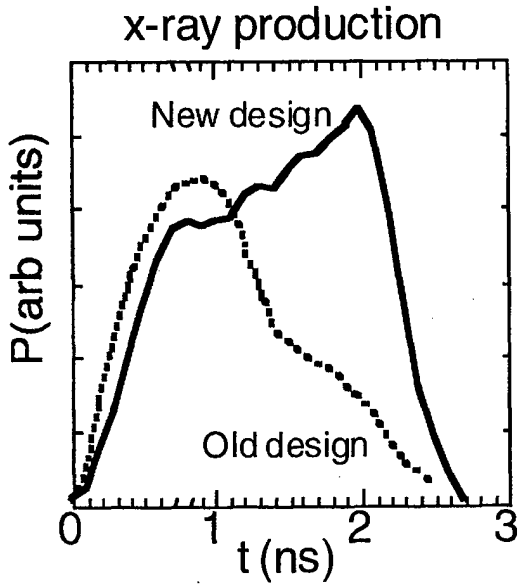

Figure 3. Predicted temporal history of the x-ray emissions from the old, small LEH design and the new, large LEH design.

the interface between the Be and Xe (cyan). This figure shows that the Be blowoff material does not impinge on the path of the laser beam.

The temporal history of the x-ray power from the new design is shown in figure 3 along with that from the old design. At early time the x-ray production is a bit less for the new design due to less confinement of the gas with the larger LEH. However, the x-ray production increases with time and last for the full 2 ns. The time integrated x-ray production is greatly improved with the new design.

The new LEH designs were the basis of the next set of experiments that were reported in the previous article. These experiments had two targets sizes both with the larger LEH

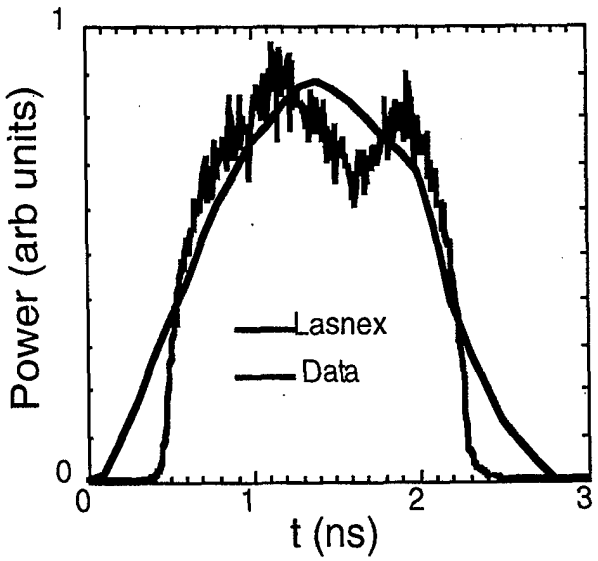

Figure 4. Comparison of the LASNEX predictions with the measured xenon L-shell emission for the large (3.6 mm diameter) can.

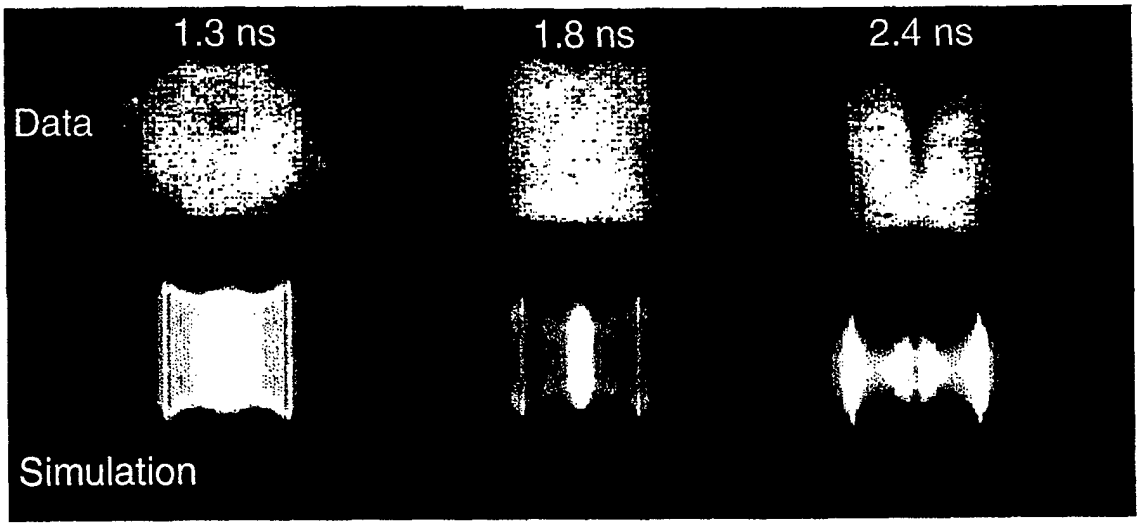

Figure 5. Side view of a beryllium hohlraum with X-ray images showing radiation with $h\nu > 4$ keV. The upper row shows the data. The lower row shows synthetic images produced by postprocessing the Lasnex simulation.

shown in figure 2. The standard size can (2 mm long x 2 mm diameter) was used along with a larger can (2 mm long x 3.6 mm diameter). The targets produced uniform emission lasting the entire duration of the laser pulse as predicted. In figure 4 we plot the x-ray emission versus time for the large can along with the predictions. The temporal history of the x-ray emission agrees quite well with the experiments. Therefore, we now believe the refraction hypothesis to be the probable cause for the discrepancies seen in the first campaign.

In Figure 5 we plot the observed spatial images of the x-ray emission as well as the emission patterns predicted by simulations. Before making comparisons it is important to note that the data no longer show the dark gaps at the center at early time. The can appears to be uniformly heated and the resulting emission pattern is uniform for the duration of the laser pulse. This is a vast improvement over the first set of experiments. This fact along with the temporal data indicates that refraction from the LEH was indeed degrading the performance of the first targets.

However, the simulations differ from the data in two distinct ways. First, the simulations predict brighter emission at the center plane. Whereas, the data seems to be more or less uniform over the can. Second, the simulations predict a tamping effect in which the ablating Be squeezes the Xe gas radially inward. The predicted x-ray emission patterns therefore get narrower with time as shown in Figure 5. In contrast, the experimental images appear to have the same height throughout the laser pulse.

In order to comment on the possible source of these discrepancies we must first understand why the simulated emission patterns appear as they do. In a coronal approximation, we can assume that the emission per unit volume scales like the electron density squared multiplied by some power (usually 1/2) of the electron temperature. The emission pattern can be understood by taking this scaling for the local emission and transporting the x-rays out of the can allowing for rotational symmetry. Therefore, in figure 6. we plot the electron temperature and the electron density at 2.0 ns. We can see that the emission at the center is

due to the stagnation shown in Figure 6. Even though there is no stagnation on axis, the rotational symmetry makes the emission appear to occur on axis.

The stagnation may be a two dimensional effect. In two-dimensional cylindrically symmetric simulations the laser spots are rings uniform around the azimuth. Therefore, the blow-off plasma is also symmetric and must converge like a cylinder. On Nova, there are five laser spots on each side of the hohlraum; the space between spots is initially comparable to the spot size itself. Thus, in the experiments in three dimensions, the plasma blow off occurs in different regions and may not accumulate in the same manner.

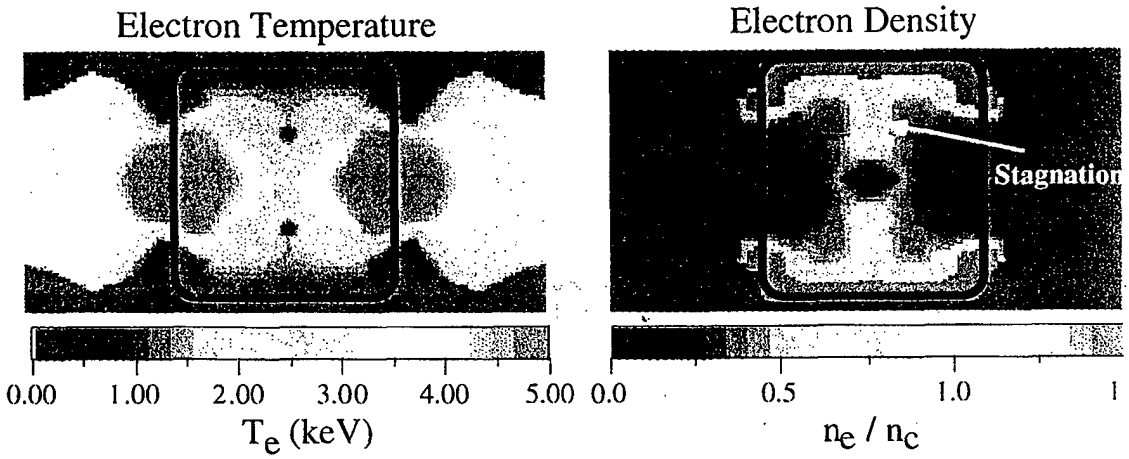

Figure 6. Lasnex images of the electron temperature in keV and electron density in units of the fraction of the critical electron density for 0.35 micron laser light, These quantities are shown for a small (radius = 2 mm) beryllium hohlraum at 2 ns, just as the laser drive beams are turning off.

Likewise the fact that the data shows no tamping may also be a three dimensional effect. With a five beams in the azimuth there are regions where there is little tamping. Therefore, the x-rays can still come from larger radii and would show very little tamping.

These discrepancies may be resolved by diagnosing the electron density and electron temperature in several regions throughout the can. In addition, three dimensional simulations would also be very useful to see how the plasma really might stagnate.

III-3. Conclusions:

Lasnex modeling has led to the design of a successful underdense radiating beryllium hohlraum filled with an L-shell xenon plasma. This correct problem was identified after examining several parameters related to the Lasnex simulations. The temporal profile of the simulations and of the measured data for the large hohlraum are in very reasonable accord. Diagnostic difficulties during the experiment prevent comparison with the emission from the smaller-radius hohlraums. There remain some qualitative and quantitative differences between the measurements and experiments. In particular, we are interested in the apparent fact that the hottest, most strongly radiating portions of the plasma in the small hohlraums, even relatively early in the laser pulse, appear near the walls of the hohlraum. This may be due to 3-dimensional effects. These are important questions to address.

IV-Hot X-Ray Output from Seed-Layer Ignition Capsules

Hot x-rays are needed for radiation effects testing on NIF. Based on LASNEX calculations, we find that it may be possible to make hot-x-ray-source ignition capsules. Two new NIF ignition capsule designs are presented. Both designs eliminate the need to seed the frozen DT. The first design adds a mid-Z seed to the ablator. The second design puts a thin layer of the seed material between the DT fuel and the ablator. This has very positive implications for target fabrication. Unoptimized results suggest that a 30 MJ ignition capsule can produce over 5MJ of x-rays above 5 keV, about 2 MJ have energies above 20 keV, and about 1 MJ are above 40 keV. We have also found that many useful x-rays are lost to absorption in standard gold hohlraum walls; alternate hohlraum designs with much less gold and lower-Z walls are being investigated.

IV-1. Introduction

We have looked at ways to increase the hot x-ray output by the modification of successful designs of NIF ignition capsules (ref. 1) This is of interest to the radiation effects community. There is an ongoing need to revalidate hardware by exposing it to fluences of x-rays above 10 keV. Without underground testing NIF will be one of very few sources able to provide the needed fluences of these x-rays.

The result is a new variant of the standard NIF ignition capsule (ref. 1) that is illustrated schematically in fig. 1. This design holds promise for more flexibility in tailoring output, producing more copious and harder x-rays. In addition, the target fabrication challenge is reduced from that of earlier designs that relied on seeding the frozen DT, to be nearly identical to that of a "standard" NIF ignition capsule. However, considerable research remains to be done on many physics issues.

We have also begun work on a modified hohlraum design. This design uses lower-Z materials since a standard gold hohlraum severely attenuates the x-rays of interest (10-30 keV). This redesigned hohlraum must have same performance as the "standard" hohlraum. We have identified the problem and are beginning work on a number of ideas.

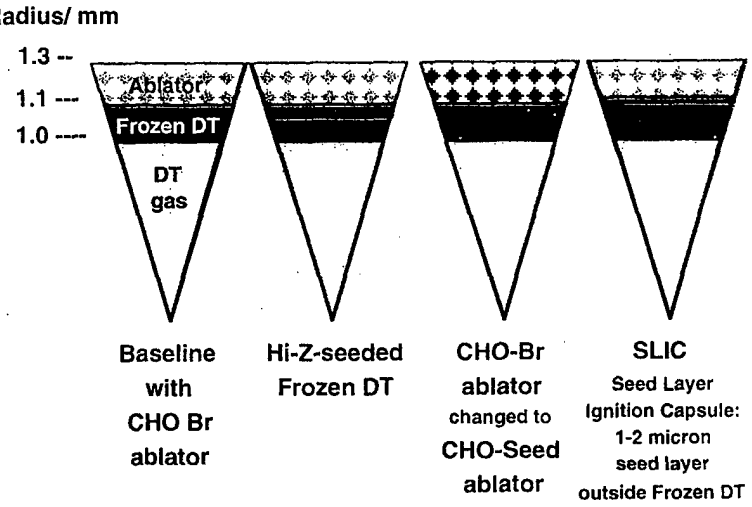

Figure 1. Schematic diagrams of the ignition capsules discussed in this section. The ablator material in most of our calculations is brominated plastic (CHO-Br for short and color-coded green in these diagrams). The indicated radii are approximate. The first capsule is the baseline that has been designed by Steve Haan of LLNL's X division and his collaborators. The remaining capsules indicate the seed material in red. The second capsule has high-Z seed material mixed into the outer third of the frozen DT (this design presents a target fabrication challenge). In the third capsule, the bromine in the ablator is replaced with a selected seed material. The fourth capsule shows the SLIC design, which stands for Seed Layer Ignition Capsule. So far, we have modeled only very thin, mid-Z seed layers. If hydrodynamic performance would be improved by adding a density gradient in a thicker seed layer, we could be compelled to move in that direction.

IV-2. The Capsule

Our capsule designs are based on designs by Steve Haan, Max Tabak, and Tom Dittrich of X Division. Our work was started on a 30 MJ capsule using a brominated plastic ablator (the first capsule in fig. 1); we are also using a 17 MJ capsule that has a copper doped beryllium (CuBe) ablator in our LASNEX calculations. The design variations evolved through three phases as shown in fig. 1. The first variation put a high-Z seed in the outer third of the DT fuel. The second variation replaced the bromine in the ablator with a mid-Z material. The third variation put a thin (~2 μm) layer of a mid-Z seed between the DT fuel and the ablator. Our best results have been obtained with the SLIC design shown in fig. 2 using a molybdenum K-shell- radiating seed layer

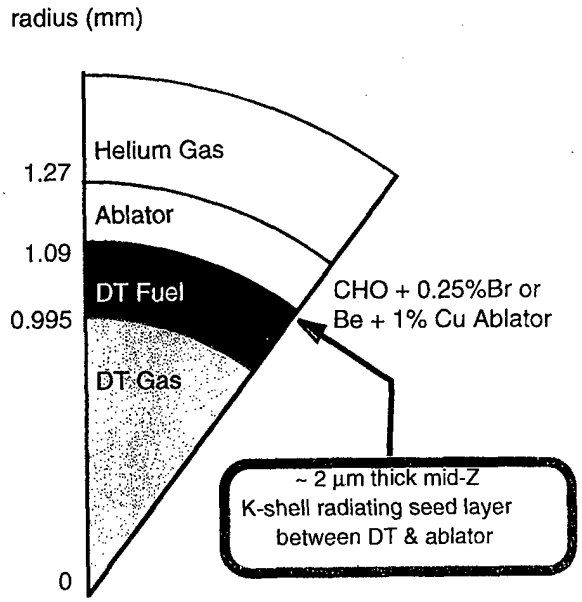

Figure 2. This pie diagram shows the structure of the brominated plastic ablator capsule.

IV-3. The Laser Drive

The laser pulse is shaped to produce a sequence of shocks that converge on the DT shell. The time-dependent drive spectrum, when converted to temperature, is shown in fig. 3. Designers adjust the time and magnitude of the various steps in the drive pulse to optimize shock convergence and capsule performance

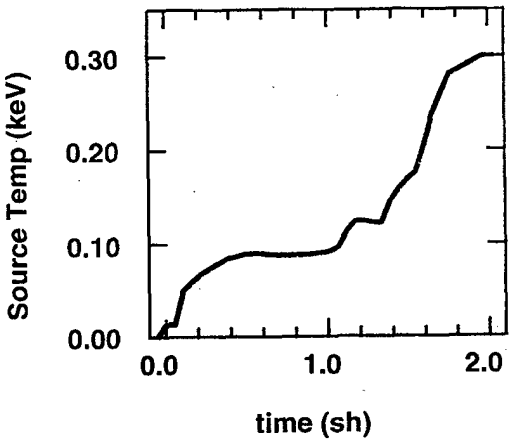

Figure 3. The temperature of the x-ray source produced by the laser drive in the hohlraum.

IV-4. Calculational Procedure

All regions out to and including the ablator were run with burn and NLTE physics turned on. The neutronics were run with multigroup diffusion.

The calculations are stopped shortly after bang time when all of the hot x-rays (> 5 keV) have been emitted. Soft x-rays with a temperature of about 100 eV and a total energy of several megajoules are emitted over a longer time span of about 100 ns. These soft x-rays are ignored for the purposes of this paper. Cold gold opacity is a good approximation of the effect of hohlraums on warm and hot x-rays ($h\nu > 5$ keV). This works since only the inner portion of the hohlraum gets hot enough to emit and its temperature is less than 1 keV. The soft x-ray attenuation is overestimated ($h\nu < 5$ keV) since the ionization of the outer shells of the gold is neglected in using cold opacities.

IV-5. Where is the emission occurring?

As we tried to diagnose our early attempts at seeding a capsule we discovered that the absorption by the gold hohlraum was masking the details of the emission by the capsule. Fig. 4 shows how the gold hohlraum walls attenuate the differential spectrum of the standard unseeded capsule with a bromine-doped plastic ablator. Note that the spectrum loses all traces of the characteristic bromine K-shell emission (just above 15 keV) as the gold thickness increases. This shows the importance of minimizing the thickness or the optical depth of the hohlraum so that the x-rays in the 10-40 keV range are not severely attenuated.

To determine the source of the emission in the capsule we put flux contours between the various regions and some within the fuel itself. By taking the difference between adjacent flux contours we determined the emission coming from a specific shell. Fig. 5 shows the emission from a 30 MJ brominated plastic ablator NIF capsule. The lower line is the emission from the DT part of the capsule while the upper line is the emission from the ablator. This result pointed out that the bulk of the emission is from the ablator, in particular from the bromine dopant that is the highest Z element present. This idea led in two directions. Previous efforts by others as well as our own first efforts put the seed into the DT fuel. As shown below this is not an optimal solution for getting hot x-rays. Next we considered a uniform dopant in the ablator. We are presently using a thin layer of an emitter between the ablator and the DT fuel. This concentrates the emitting atoms in the region outside the DT itself that gets the hottest. This should promote the emission of hot x-rays.

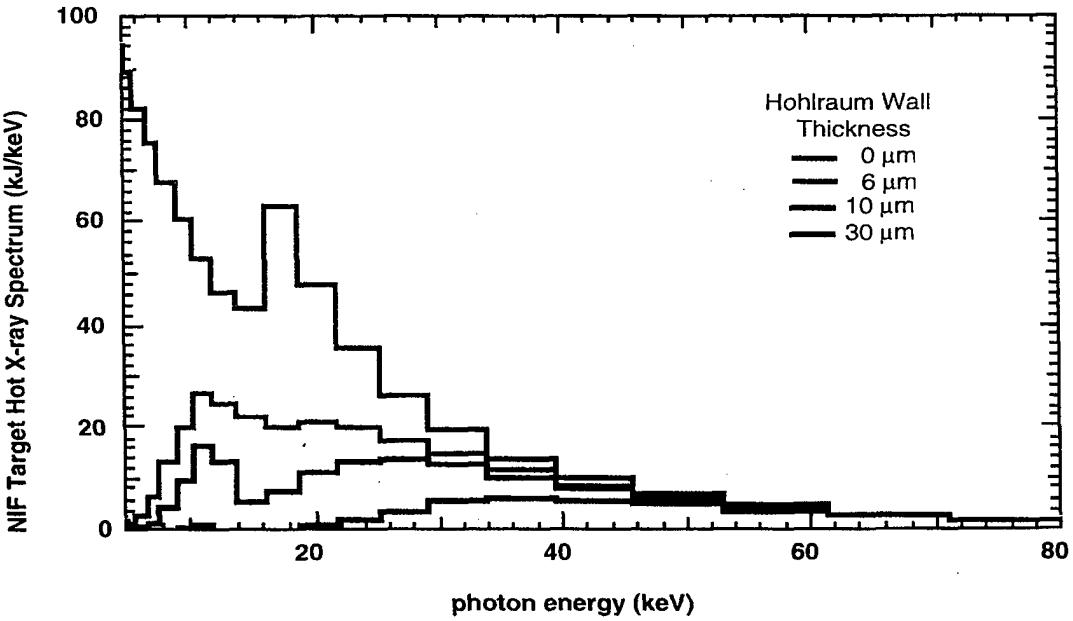

Figure 4. The dependence of the ignition-target output spectrum on the thickness of the gold hohlraum. Cold gold opacities are used to illustrate how the absorption by the gold hohlraum wall completely obscures K-shell emission (~15 keV) of the bromine in the ablator. Cold opacities are representative of the actual wall absorption for the hotter photons of interest to this work. Note that the abscissa begins at 5 keV.

IV-6. Seeding strategies

1. Seeding the DT fuel

Initially we looked into ways to dope the DT fuel to produce more x-rays. This is illustrated in the second design schematic of fig. 1. This concept, which has been explored by a number of researchers from both X and A Divisions, seeds the outer third of the frozen DT with a high-Z element such as uranium. However, DT seeding poses significant target fabrication challenges. Fig. 6 shows the enhancement achieved when the outer third of the DT fuel is seeded with 0.005 atom fraction of uranium. Even here we also notice that the brominated ablator contributes significantly to the emission.

The reason for seeding the DT is that this is the hottest material in the capsule. Only the outer third of the DT is seeded so that the seed material won't mix into the central hot spot. This would prevent the capsule from igniting. Seeding the outer third of the fuel with 5 parts per thousand of uranium reduced the total capsule yield by a factor of one third.

Looking at the energy production in more detail revealed that a high-Z seed duds most of the energy production in that region. Fig. 7 compares the energy production in the fuel for the unseeded and seeded cases. The propagating burn is evident in the high-Z seeded DT layer but the energy production rate is greatly reduced from the unseeded case.

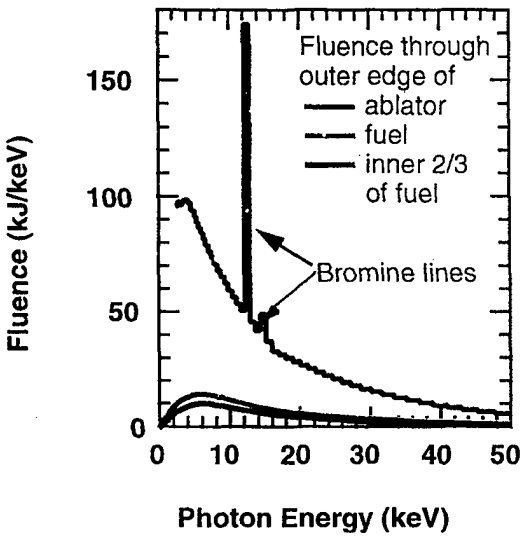

Figure 5. The emission from a 30 MJ NIF ignition capsule (brominated plastic ablator) is plotted. The fluence from the DT fuel is much smaller than the fluence from the ablator.

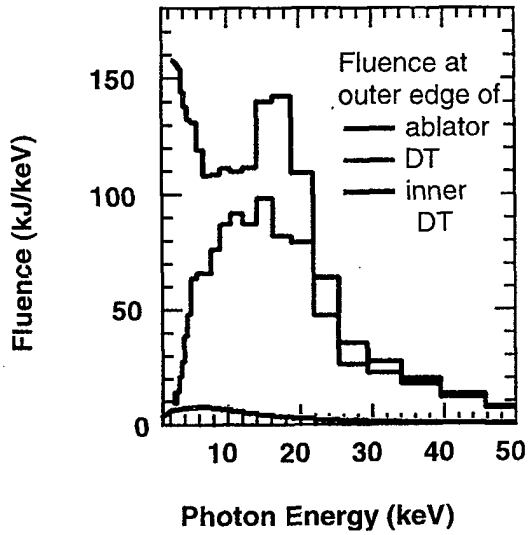

Figure 6. The emission from a 30 MJ NIF ignition capsule (brominated plastic ablator). The outer third of the DT fuel was seeded with 5 ppt of uranium The emission has been broken up to show the contributions from the ablator, the seeded fuel, and the unseeded DT fuel.

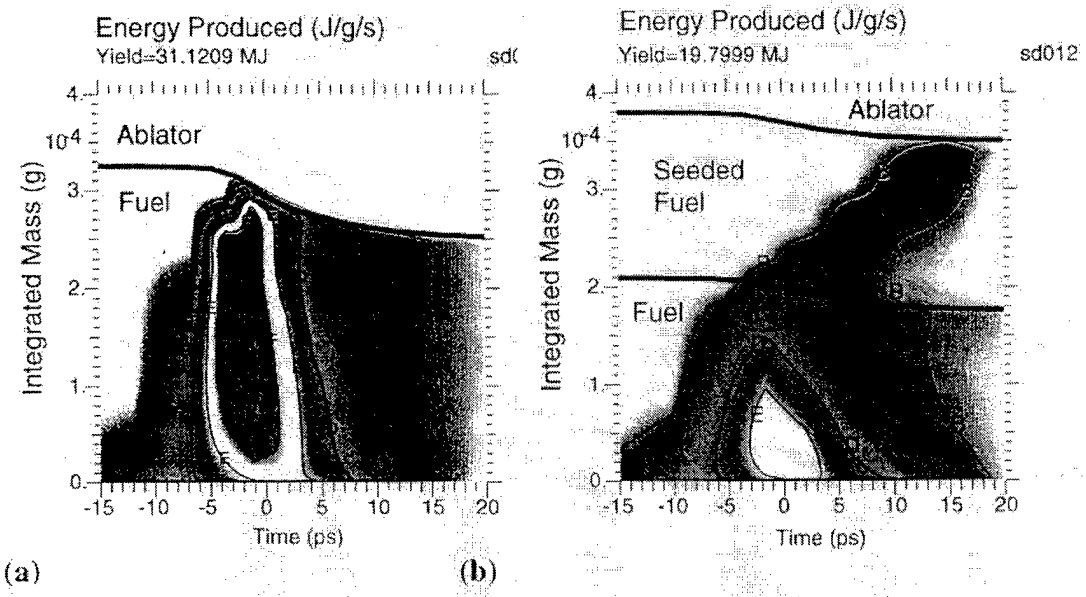

Figure 7. Energy production as a function of time and mass integrated out from the center. (a) The unseeded capsule. (b) A capsule with 5 ppt uranium in the outer third of the DT fuel. The horizontal black lines denote the edges of the DT fuel and the interface between the seeded and unseeded portions of the DT. The interface decreases in mass due to the burning of the DT.

2. Seeding the ablator

Since the bromine (Z=35) that is normally in the ablator is the dominant sources of hot x-rays in the standard NIF capsule we replaced the bromine with higher-Z elements. This is illustrated in the third schematic design in fig. 1. We looked at strontium, molybdenum, tin, neodymium, and ytterbium with Z=38, 42, 50, 60, and 70, respectively. Table 1 lists and Fig. 8 shows the cumulative fluences from these calculations. The hot x-ray output tends to increase with the Z of the seed. Except for the tin and molybdenum calculations they all share a common high energy tail to the spectra. For each spectrum there is an increase in x-rays at the region of characteristic K-shell emission for the seed element (the cold K edges are at 13.5, 29.2, 43.6, 61.3 keV for Br, Sn, Nd, and Yb respectively). The spectra show that the strength of the K-shell emission is declining rapidly as Z increases which is consistent with the ionization distribution of the ablator seed material during the time of emission.

These calculations were run with NLTE physics turned on. For some reason unknown to us at this time the tin and molybdenum calculations fall far below the others. There is no obvious reason for this and we are continuing to investigate it in case there is a problem with the NLTE opacity package for tin. Part of the problem shows up as a reduction in yield. This can be caused by windows in the opacity of the seed ruining the timing of the shocks or by heating the fuel excessively.

Table 1. The x-ray energy (MJ) emitted above a cutoff by a seeded ablator with no hohlraum absorption.

	Seed (in ablator)					
Cutoff Energy	**None**	**Sr**	**Mo**	**Sn**	**Nd**	**Yb**
5 keV	1.42	1.46	0.38	1.55	2.60	2.96
20 keV	0.55	1.17	0.08	0.46	0.76	0.88
Yield	31.0	30.4	10.7	24.4	26.0	31.5

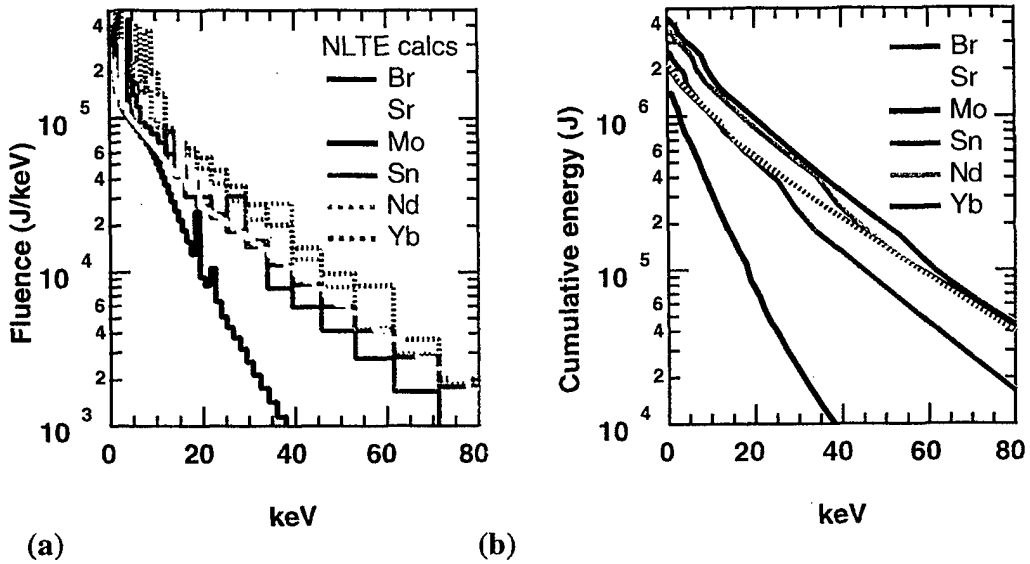

Figure 8. The spectra, (a), cumulative fluences, (b), from 30 MJ NIF capsules with different seeds in the plastic ablator. It is not yet known why the molybdenum calculation had a yield so much lower than the others (see Table 1).

3. Seed layer between the fuel and ablator

It is only a thin layer on the inner edge of the ablator that gets hot enough to emit the energetic x-rays. Fig. 9 shows how thin this layer is for the standard brominated ablator. Only the inner 30 μm (~0.4 mg) of the ablator has the bromine stripped down to the K-shell. In an effort to increase the amount of hot, K-shell radiating material, we next tried putting a layer of the seed material between the DT and the ablator.

IV-7. Results from Thin Seed Layers

Using thin seed layers is the most flexible scheme we have come up with so far. This is the fourth design in fig. 1. These results are preliminary; we have not optimized the layer thickness and have only tried single element seeds. We predict K-shell emission for elements with Z≤50. Tables 2 and 3 show the results for this design. Table 2 and Fig. 10 are the results for the bare capsule. Table 3 and Fig. 11 include absorption by 10 μm of cold gold to simulate a thin hohlraum. When only the capsule emission is considered (Tab. 2) a silver seed layer produces the most hot x-rays among the mid-Z K-shell emitting

seeds. Table 3 shows that a molybdenum seed layer produces the most hot x-rays when the attenuation by a 10 μm gold hohlraum is included.

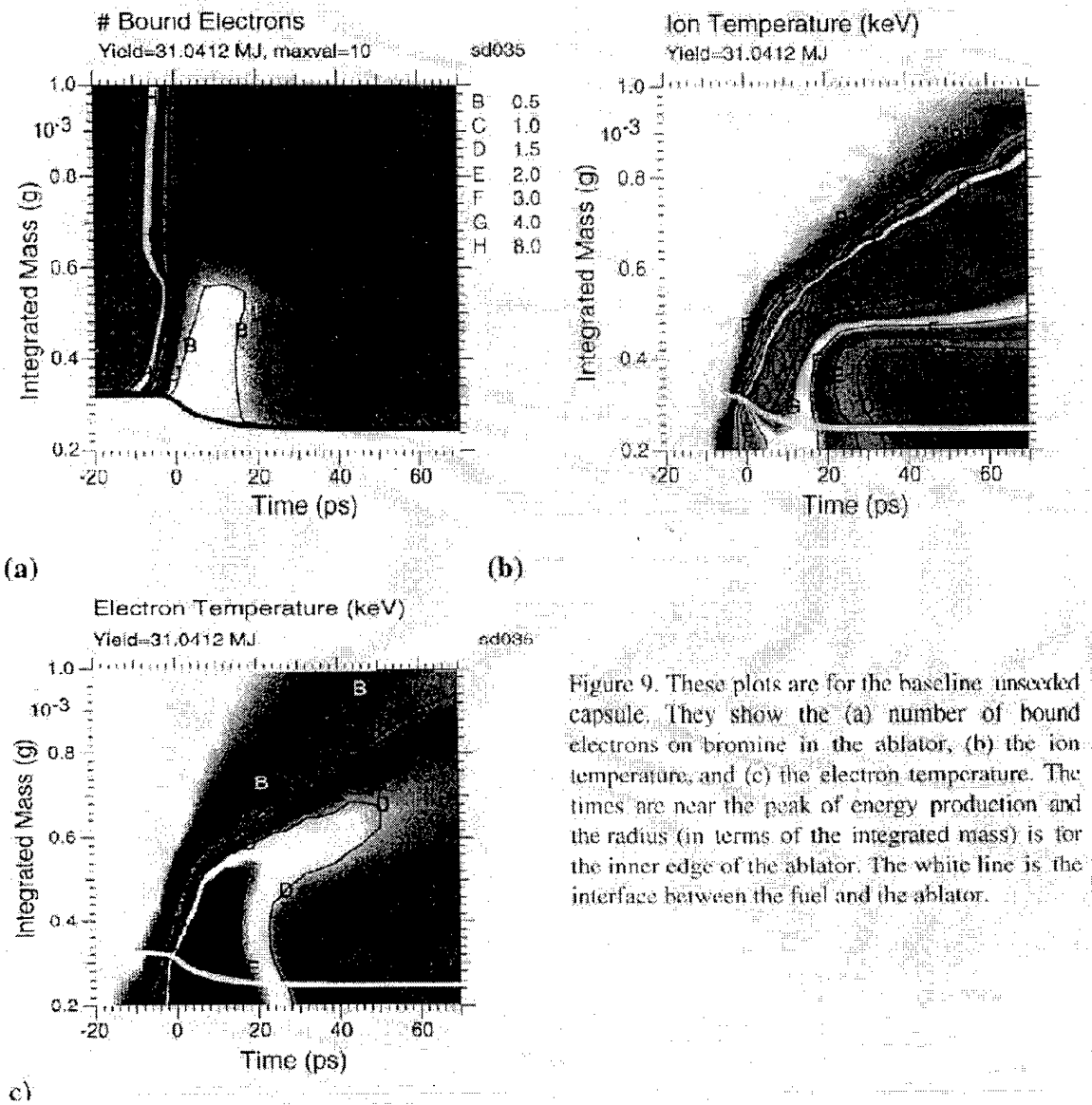

Figure 9. These plots are for the baseline unseeded capsule. They show the (a) number of bound electrons on bromine in the ablator, (b) the ion temperature, and (c) the electron temperature. The times are near the peak of energy production and the radius (in terms of the integrated mass) is for the inner edge of the ablator. The white line is the interface between the fuel and the ablator.

Table 2. The x-ray energy (MJ) emitted by Seed-Layer Ignition Capsules (SLIC) above a cutoff with no absorption by the hohlraum.

	Seed (1.7 μm layer)					
Cutoff Energy	**None**	**Br**	**Mo**	**Ag**	**Sn**	**Xe**
5 keV	1.42	2.96	3.46	3.65	3.17	2.33
20 keV	0.55	1.17	1.31	1.39	1.16	0.68

Table 3. The x-ray energy (MJ) emitted above a cutoff attenuated by a 10 μm gold hohlraum.

	Seed (1.7 μm layer)					
Cutoff Energy	None	Br	Mo	Ag	Sn	Xe
5 keV	0.43	0.81	0.99	0.95	0.80	0.49
20 keV	0.37	0.68	0.82	0.77	0.64	0.37

IV-8. Conditions in the seed layer

Fig. 12 depicts conditions in a seed layer of molybdenum. The time axis is centered on the time of peak energy production. Note that the molybdenum is stripped into the K-shell right after the peak of energy production. Fig. 12b shows that the molybdenum is colder than the DT fuel. Its peak electron temperature is about 12 keV; much less than in the DT fuel. The temperature is lower since the molybdenum (with more electrons available) radiates more efficiently than the DT fuel. Fig. 12c shows the mass decrease in the DT fuel due to burn. You can also see that the mass of the seed layer increases during burn; this is due to alpha particles that are stopped in the molybdenum. This is one source of heating for this layer.

IV-9. Conclusions

The scheme of putting mid-Z seed between the fuel and the ablator is a robust way of producing hot x-rays. These Seed-Layer Ignition Capsules avoid the problem of reduced yields that occurs when the outer part of the DT is seeded. It also will be easier to fabricate targets like this. We have preliminary results for CuBe ablator targets. Unoptimized, preliminary results suggest that a 34 MJ ignition capsule can produce over 4 MJ of x-rays over 5 keV and well over 1 MJ have energy greater than 20 keV. The results are similar to the plastic ablator capsules for some cases. However, we find that these CuBe capsules appear to be more sensitive to the seed layer preheating the fuel and decreasing the yield.
There are numerous issues that remain to be addressed. Among these are:

- Rayleigh-Taylor hydrodynamic instabilities at the ablator-DT interface (which may decrease or may increase the hot x-ray emission). Mixing of the seed into the fuel will tend to decrease the yield and hot x-ray emission. The convoluted interface between the seed and the fuel will have a larger surface area and will decrease the density of the seed; this will tend to decrease the emission as well. If unmixed seed is surrounded by burning DT then emission may increase.
- The NLTE physics that governs emission in the seed layer. One possible issue is that it may be inaccurate for very thin layers.
- Energy transport from the DT ignition region into the seed layer and the ablator.
- Target-fabrication remains a concern but is reduced to being very similar to those of the standard NIF fusion capsule.

The gold hohlraum can absorb a significant fraction of the interesting X rays that are produced. Replacing the gold in the hohlraum with a material that has similar low-Z opacity, *e.g.* FeS_2, would allow more of the x-rays above 5 keV to escape. Another option would be to put a low-Z window material in a portion of the hohlraum to allow the x-rays to escape. A third option is to use a thin Au layer tamped by a low-Z material.

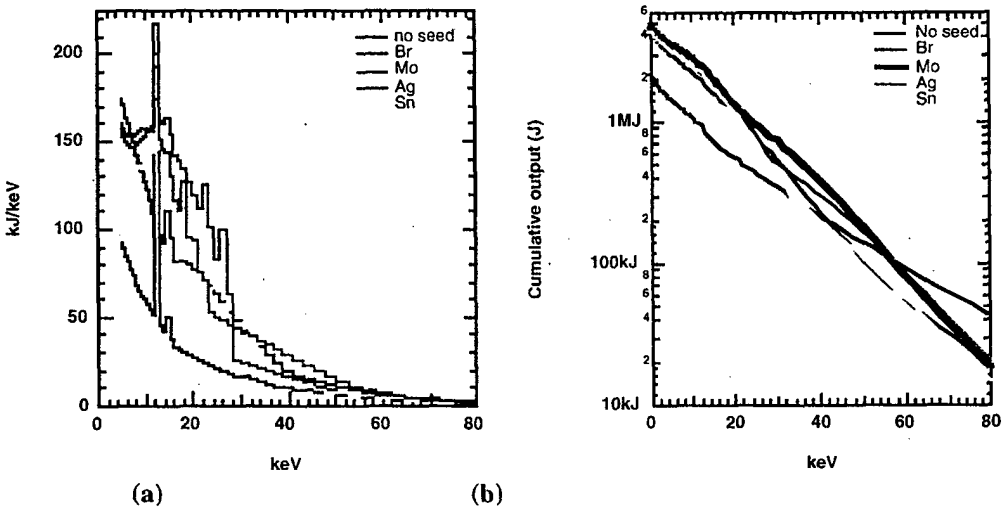

Figure 10. The differential spectra (a) and cumulative fluence (b) emitted by the seed-layer ignition capsule (SLIC) when different single-element seeds (1.7 μm thick) are put between the fuel and the ablator.

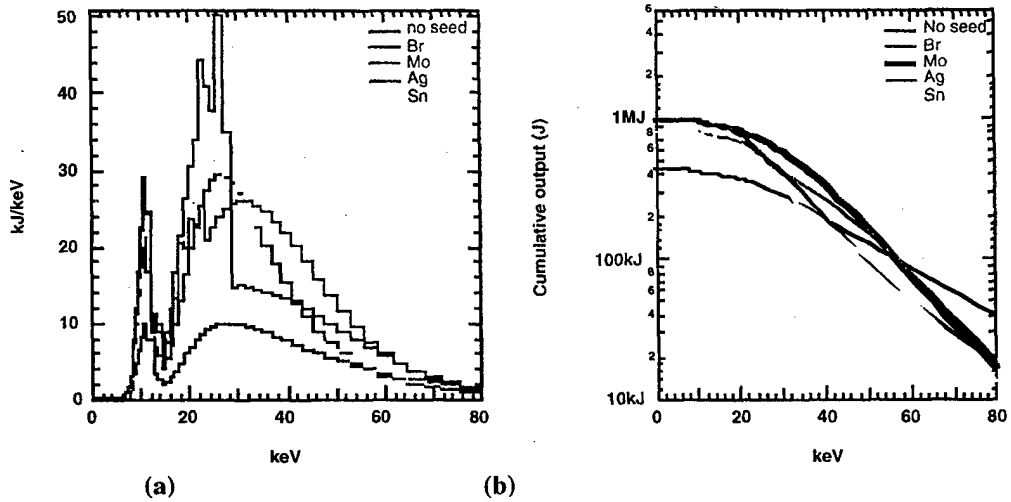

Figure 11. Capsule outputs of fig. 10 above where the spectra have been attenuated by 10 μm of gold to simulate the effect of a thin hohlraum on the emission.

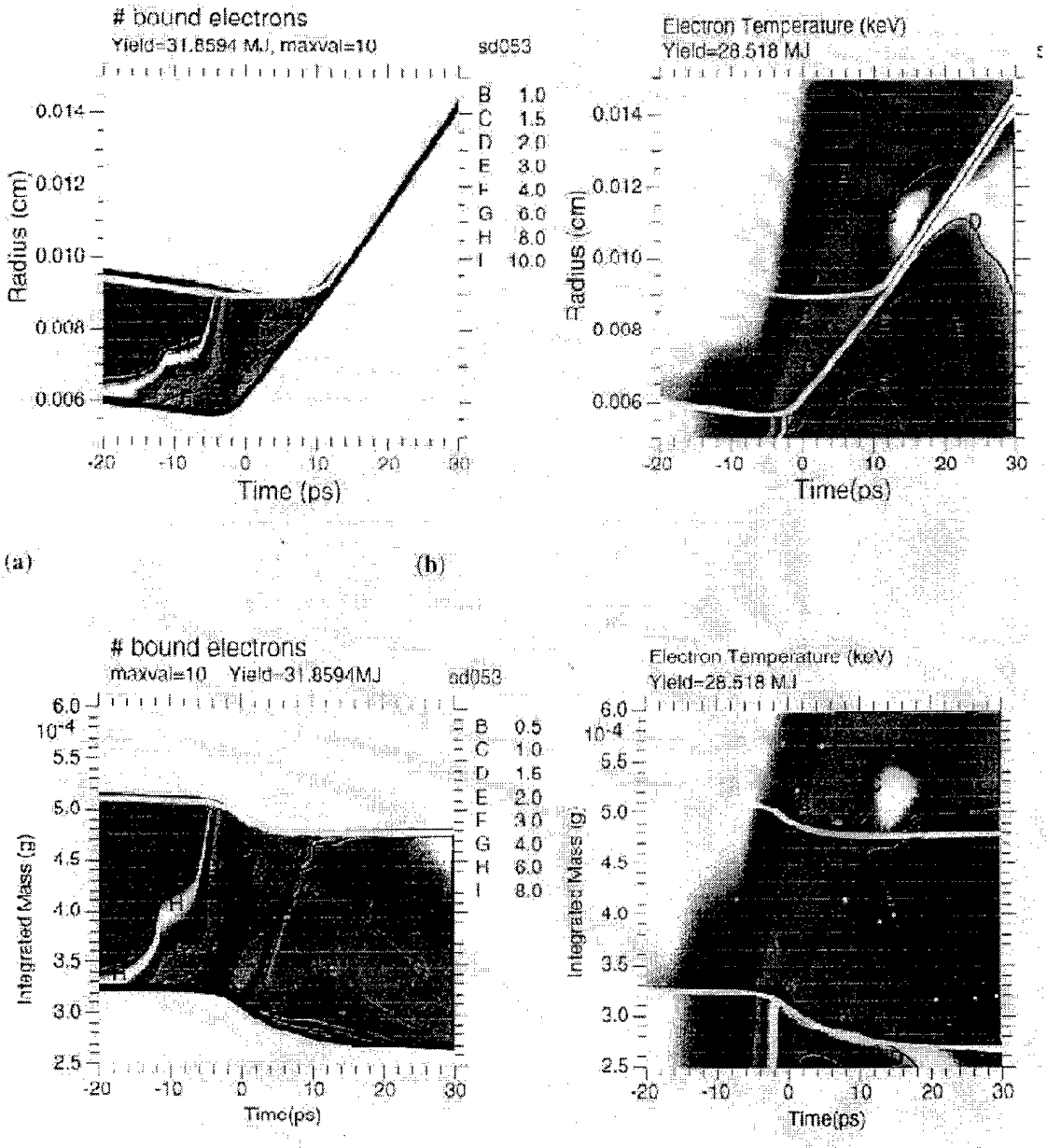

Figure 12. The number of bound electrons, (a) & (c), and the electron temperature, (b) & (d), of the seed layer as a function of radius, (a) & (b), and integrated mass, (c) & (d). There is a large reduction in time resolution at 26 ps.

IV-10. References

1) Haan, S. W., *et al.*, "*Ignition Target Design for the National Ignition Facility*," ICF Quarterly Report, July-Sept. 1995, Lawrence Livermore National Laboratory, Livermore, CA, USA, UCRL–LR–105821–95–4, (1995).

2)S. Carman and J. Heidrich, "Neutron and X-Ray Output Obtained from Preliminary Calculations for Enhanced X-Ray Output of Indirect Drive ICF Capsules (U)," *Defense Research Review*, **V6, #2**, 17 (1994), UCRL 53880-6-2.

3) Back, Decker, DiPeso, Gerassimenko, Managan, Serduke, Simonson, and Suter, "High-Power Laser Source Evaluation," Lawrence Livermore National Laboratory, Livermore, CA, USA UCRL-ID-129096.

V-Review and Status of Facilitization for NWET on NIF

V-1. Requested Modifications in the NIF Design

In January 1996, the NIF Radiation Sciences Users Group (NRSUG) drafted suggested changes to the NIF Primary Criteria /Functional Requirements to support radiation effects test capability. These suggestions resulted in the approval of Baseline Change Proposal 96-005. This request 'Not to Preclude Radiation Testing' was approved on May 1, 1996 by the Level I Baseline Change Control Board. A synopsis of the requested changes in the NIF Functional Requirements and Primary Criteria to accommodate the requests of the NRSUG includes the following items:

1) the baseline design and operation should be capable of performing radiation effects testing,
2) there should be a higher shot rate to accommodate multiple user requests,
3) 1ω and/or 2ω operation should not be precluded,
4) there should be flexibility in beam focusing and pointing,
5) the basic capability for distributed sources is to be provided.

V-2. Status of the Requested NIF Design Modifications

Significant gains have been made over the past year in specification of the NRSUG requested modifications to the NIF design to accommodate radiation effects testing. This section is intended to provide the status of the facilitization of the NIF to support radiation effects testing as of December 1997. In January 1996, the DOE/ONIF directed the NIF Project Office to develop a response to the NRSUG requested modifications to the NIF design. This led to the NIF Baseline Design Change Proposal 97-005 that provided 'Not to Preclude Radiation Testing'.

A 'not-to-preclude' or 'provide capability' design requirement is a requirement that must be achieved and may have cost to implement outside of project cost. To satisfy this requirement, a NIF Project engineer must be able to show that additional hardware can be added after the initial construction phase is complete with an acceptable schedule impact. The Project engineer's primary mission is to design the NIF for its intended mission. Many of the 'not-to-preclude' or 'provide capability' design requirements will, therefore,

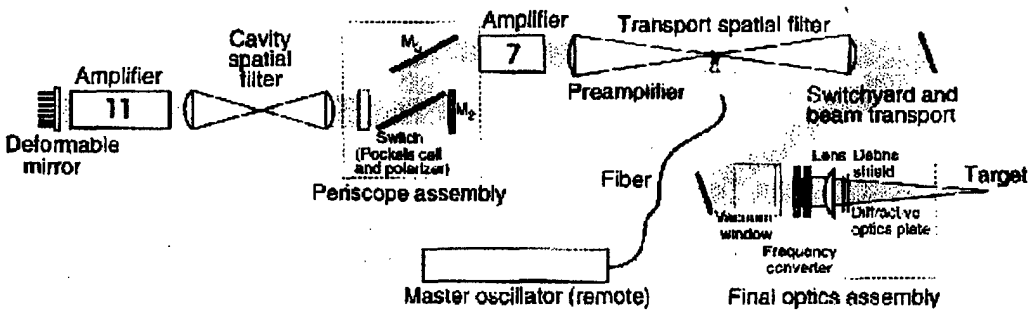

Figure 1 Schematic of the NIF 11-7 amplifier configuration

entail risk on our (the NRSUG) part for this requirement unless risk mitigation studies/engineering are performed. The status of all the requested modifications to the NIF design will be discussed in the following sections.

V-3. Laser System

At the end of Title I design (Nov. 1996) the NIF Project determined that the NIF baseline performance requirements can be met with an 11-5 amplifier configuration and with 48 pre-amplifier modules (PAMs). A basic schematic diagram of the 11-7 NIF laser system is shown in Figure 1. This 11-5 amplifier configuration represents a reduction in the total number of amplifier slabs relative to the CDR design. The performance margin will be less than for the 11-7 arrangement, thus component performance is more critical and energy / power will be less for stressing operation conditions. This would include our desire to have the maximum energy from the system. Two amplifier slabs and 48 PAMs can be added later if required to recover performance margin. The calculated NIF 3ω performance envelope is shown in Figure 2. Note that close to 3 MJ of 3ω laser light may be possible at an 8 ns pulse width.

V-4. Design Changes that Affect NWET Facilitization

The change in the number of PAMs has resulted in loss of laser system versatility that directly affects flexibility in effects test scenarios. This includes loss of laser performance options such as: more than one color within each beam quad; different pulse shapes within each beam quad; and potential loss of time delay within each beam quad. Different colors, pulse shape or time delay between quads is not precluded. The use of 48 PAMs will limit the maximum output energy from the laser, thus providing a reduced upper limit of source strength. This may also have a detrimental effect on the ability to use 1ω sources. Previous studies have shown that one option in the use of distributed sources may cause some beams to be clipped at the chamber port; this would require some beams to be apertured. This was to be accomplished by an insertable aperture in the PAM. With 48 PAMs, if a beam needs to be apertured, then all the beams in that quad would also be identically apertured leading to less energy on target for the same laser power density/unit area. An alternative is to steer the potentially-clipped beam, via an appropriate diffractive optic, to a second target. With 48 PAMs, there can be only limited time delay or power difference between beams in a quad, so this latter option restricts

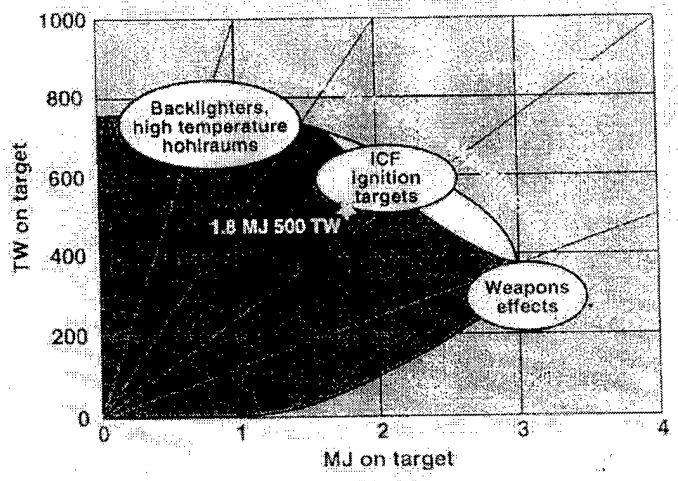

Figure 2. The projected NIF 3ω performance envelope for power and energy delivered to targets. Note that it is possible for NIF to deliver about 3 MJ of blue light in an 8 ns pulse.

options of x-ray output pulse shaping by irradiating targets at different times and/or power. The Pre-Amplifier Transport System (PATS) will allow some fine tuning of the power and delay (10 ns total).

V-5. Pulse stacking, long pulse shapes

The NRSUG requested a time delay in order to stack laser beams to cover a broad range of x-ray output temporal pulse shapes. The NIF design allows delay from the first to last laser beam timing of order 30 ns via operator control with the option of longer delays to order 100 ns. This time delay is in the PAM and/or 'trombone' section near the PAM injection point to the main amplifiers. The use of only 48 PAMs will limit the flexibility of the laser to effectively 48 independent systems (quads). The NIF Project design of the optical pulse generation system will allow an operator selected range of 10 ns for a 'Haan' pulse (the shaped NIF pulse that will ignite the indirect-drive NIF fusion capsules). Note that a 'Haan' pulse is approximately 20 ns, thus a nominal laser pulse width of 3-5 ns will have an operator-selectable range of about 25 ns.

The option to have variable pulse shapes and long pulse widths to accommodate source requirements for effects testing is in the system design for each quad and there is no incremental cost for having the 25 ns selectable range. The implementation of a larger range of pulse delay will require a change in the Master Oscillator Room (MOR). This change will be relatively simple to implement as the pulse timing system in the MOR will allow fiber optic solid state switching between a standard fiber or a delay fiber. This will only require changing out the fiber optic lengths in the Optical Pulse Generator (OPG). The cost of the fiber optic and installation would be borne by the user community, however, some quads will have delay options set by the need for backlighters or other special target configurations. Longer inter-beam time delays could then be implemented via NIF operator control of the optical switches in the Master Oscillator Room to the longer fibers. The replacement or installation of NRSUG specified fiber optic lengths is, in the present design, straightforward and can be implemented with no impact on standard NIF operations.

No further action is required from the NRSUG to protect this option at this status level, however, the NRSUG must remain active in protecting its interests. There is no additional impact on the NIF design, construction or operation.

V-6. 1ω /2ω Operations: Suprathermal electron bremsstrahlung

1.06 micron (1ω) laser irradiation of hohlraum-like targets shows promise of producing a usefully-large population of hot electrons (T_e~60 keV) that can subsequently interact with the high-Z hohlraum target walls to produce bremsstrahlung radiation. The previous assessment by DSWA and the NIF Radiation Sciences Users Group has indicated that x rays with $h\nu$ > 25 keV generated in Stimulated-Raman-Scattering (SRS) -dominated hohlraums would be of high utility for high fidelity (threat-like) radiation effects testing of strategic electronic systems and components. The projected source intensity, spectral fidelity and temporal fidelity all appear attractive for weapons effects test applications. This assessment has assumed 3 MJ of 1ω laser beams onto an array of targets, possibly distributed as much as ±25 cm from the target chamber center. The ability to focus 1ω to targets is protected in a 'not to preclude' statement in the Function Requirements/Primary Criteria.

The primary issue for conversion to 1ω operation is to ensure that no back reflections from the target or other target area hardware into the acceptance cone of the final spatial filter (FSP) are of sufficient magnitude to be amplified back up a still-energized laser chain and cause major damage to the laser amplifiers and mirrors. This is of concern to the NIF Project and the use of unconverted 1.06 μm light to produce these x-ray sources might require additional isolation. Additional isolation would be expensive to implement and would, if required, dampen interest in using this potential test capability. Recently it was suggested by E. Michael Campbell and Bill Kruer (internal LLNL memo of 16 June 97) that hard x-ray production with 2ω irradiation may be useful and of less risk. Recent experiments by Brian MacGowan have shown significant generation of suprathermal electrons by 3ω light. A full assessment of the potential risks, cost and test utility of any of these approaches needs to be considered, preferably before the end of Title II design. The NRSUG needs additional information fully to assess this potential test capability of the NIF: the cost to implement; operational risks; shot costs (effectively, to the user); and, also, the potential impact of this type of test on the availability of the NIF for other effects testing.

V-7. 1ω operation

At issue is, can the NIF be operated safely at 1ω at high power with the operational configuration desired by the test community? What are the limitations? From the test perspective, will it be cost-effective, are there limitations on the NIF performance envelope, and will the resultant test environment be of interest to the test community from the viewpoint of cost and availability? John Murray, the NIF Project Chief Scientist for 1ω has suggested an inexpensive option for protecting the NIF laser amplifiers that would utilize long laser pulse shapes to deplete the energy in the amplifier slabs, thereby preventing amplification of unwanted reflections. It is reasoned that this proposed operational mode would allow safe NIF operation at 1ω. However, this option needs to be examined carefully to consider all components in the laser chain and to also consider impacts to the NIF operation. One issue, since the number of PAMs has been reduced to 48, is whether there is sufficient energy in a long injection pulse to effectively deplete the energy in the amplifiers. Perhaps a proof test with the 1st bundle to the target chambers in 2001-2 would be possible. The downside of this suggestion includes issues of the target response to long pulses and the acceptability of the resultant x-ray pulse shape to the test community.

V-8. The 2ω option

The NIF Project believes that the use of 1ω entails risk to the laser. It has been proposed that efficient hot electron generation might be obtained with optimized targets using 2ω, thus eliminating the risks associated with focusing 1ω. The expected efficiency for hot electron generation could be obtained with targets optimized where SRS and two-plasmon-decay instabilities become efficient. High conversion efficiencies (-50%) of incident laser light to hot electrons might be possible.

A deeper understanding of the underlying physical processes as well as further modeling and Nova experiments to better assess the possibilities are needed. However, 2ω operation my also pose some risk to NIF operations. For example, John Murray suggests a careful examination of possible 2ω reflections at the KDP interfaces as they may result in

undesirable conditions at the turning mirrors or ghosts in the up-beam optics. From an effects test view, this potential option opens up a different NIF operational scenario with different optical components. However, the basic operational scenario would remain the same. Distributed 2ω targets would also be as far as 25 cm from the target chamber center and NIF operation would also require 192 focusing and diffractive optic elements to be inserted at the debris shield location. All issues of full energy 2ω operation need to be considered.

V-9. Potential Test Scenarios

The original assessment assumed the use of 1ω at about the maximum available energy (assumed to be 3 MJ by detuning the KDP). John Murray indicated that this is a good number to work with assuming a 6-8 ns pulse width. For 2ω operation, the KDP would be detuned to maximize 2ω operation and the available energy would be about 20-30% less.

Test scenarios for either 1ω or 2ω operation would use multiple-target arrays of individual sources. Some would be as far as 25 cm from the target chamber center (possibly further) in a plane in front of a test object to increase the effective source solid angle. Beam steering and focusing of 1ω/2ω to SRS dominated targets that are potentially away from target chamber center would be with a diffractive optic to be inserted in the replaceable debris cassette behind the debris shield (in the final optics assembly). Thus, effects testing with 1ω/2ω would require the insertion of 192 diffractive optics, detuning the KDP crystals and focusing to the distributed array.

There is a near-term need to evaluate the 1ω and 2ω options on NIF. A joint program to evaluate 1ω, 2ω and 3ω produced hot-electron bremsstrahlung sources is proposed between LLNL and DSWA. Among the goals of the program are the following:

a) carefully evaluate the 1ω option,
b) explore efficient hot electron production on Nova at 2ω and 3ω.
c) look at target design enhancements for 1ω, 2ω, and 3ω,
d) answer questions on fielding, NIF operations, and risk to the laser,
e) perform a cost-performance-test utility tradeoff study for the three options.

It should be noted that interest in suprathermal-electron bremsstrahlung sources and 1ω operation is not limited to the NWET community. The need for more energetic backlighters to permit imaging of the larger experimental packages that will be fielded on NIF has compelled Weapons Physics experimenters to consider driving hot-electron backlighters with several 1ω beams.

V-10. Distributed Sources

1. Diffractive Optics

Since laser target x-ray sources can and will be made up of many individual sources, this allows the consideration of sources to be distributed spatially and has significant payoff in potential test capability. The biggest payoff is in the larger test areas of uniform fluence compared to a point source of the same total energy. A coordinated program to look at various source configurations has just begun in order to optimize distributed sources for fluence uniformity and beam pointing/focusing considerations.

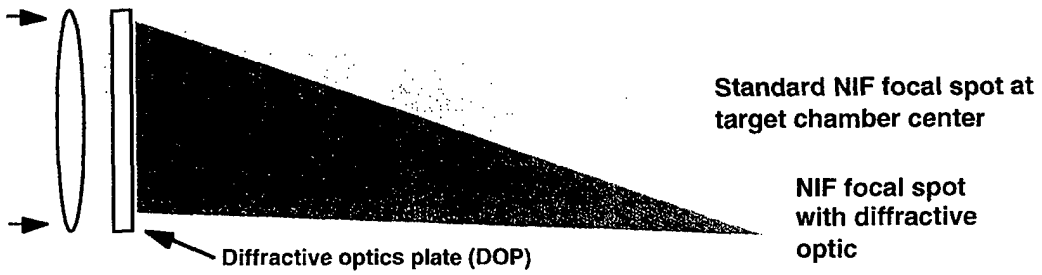

Figure 3. The effect we are seeking from our long-focal-length diffractive optic corrector lenses that will shift the focal point of any NIF beam so that target-array sources can be fielded.

It is the responsibility of the NIF Design 'to provide the basic capability of distributed sources.' However, it is the effects community that must try to ensure that this capability is protected in a usable, efficient, manner with minimum cost to implement. The present design of the Final Optical Assembly (FOA) and it components accomplishes these goals. Due to risks to the laser system and final optics as determined by the NIF Project, diffractive optics will be used for all laser wavelength steering and focusing to distributed arrays. This technique for steering and focusing for NRSUG target arrays is to be accomplished by a replaceable Diffractive Optic Plate (DOP).

The present design of the Final Optical Assemblies is shown in Figure 4. Included in the design as subassemblies are a Final Optic Cell (FOC) and a replaceable debris shield cassette. The FOC includes the frequency conversion crystals, the focus lens, and a space for a diffractive optics plate. The NIF design will use a color separation grating in the FOC to manage unconverted light. The FOC is considered a Line Replaceable Unit (LRU) for NIF maintenance, thus its design will allow replacement within normal maintenance procedures. However, it is not expected to require significant maintenance. The debris shield will require periodic cleaning which will be a function of the shot history. The debris shield system is designed as a line replaceable unit for weekly maintenance, with the change out of all 192 units to occur in one work shift (8 hours). Thus inclusion of the Diffractive Optic Plate in the debris shield cassette will allow ease of installation and replacement. The use of the color separation grating, its design and this technology development for the NIF baseline are significant as they benefit the possible use of similar optics for distributed sources. The timely utilization of this technology and design would undoubtedly save resources and time from what would be required in the future to develop the technology for distributed sources. The optimum time would be towards the end of Title II when the optics design team could devote time and resources to distributed source issues. A individual diffractive optic plate is estimated to be about $20K, depending on its complexity. Thus, a full complement for a distributed source array (200) is estimated to cost $4M.

2. Apertures in the PAMs

A preliminary look at the beam steering angle and change of focus requirements of a 50 cm square array with 25 evenly distributed targets has been performed. This study would indicate that at the maximum beam steer considered of 25 cm from the target chamber center, several of the beams of a quad (2x2 beam) appears to be clipped at the target chamber port, thus an estimated quad energy loss of about 10%. To 'not preclude' beam steering to ±25 cm and to prevent laser damage and scattered light problems from laser light

hitting inside the Final Optical Assembly, provisions for an aperture has been designed in the Pre-Amplifier Module (PAM). The present facility design will use only 48 PAMs ('not to preclude' 96) which implies that if one of the beams in a 2x2 beamline must be apertured then all four beams will be identically apertured. The implications of this limitation needs further study and complete targeting scenarios for a variety of target arrays is being conducted.

Two operator-interchangeable apertures are designed to be in the PAM. These will be in the beam shaper inside the PAM. One of interchangeable apertures is to 'not preclude' beam steering to ±25 cm. The NIF Project has requested that the aperture be specified in the Title II design or a blank will be installed. To install the appropriate aperture after the PAM is built and installed will be a somewhat intensive and expensive effort. Each PAM will need to be removed from the NIF laser system, opened in a Class 100 clean area, the new aperture installed and the modified PAM reinstalled in the Laser system. This is estimated to be a time intensive, costly process. If possible it is recommended that we identify several distributed target arrays, and the required beam focusing and steering, then use this information to specify an aperture set for the PAMs.

V-11. Target Area

The Target Area and the Conventional Systems encompass the majority of the requested changes in the NIF design to accommodate radiation effects testing. The present design of the Target Area and the Diagnostic Support Building appears adequate for large test object access and use. Figure 5 shows a schematic of the

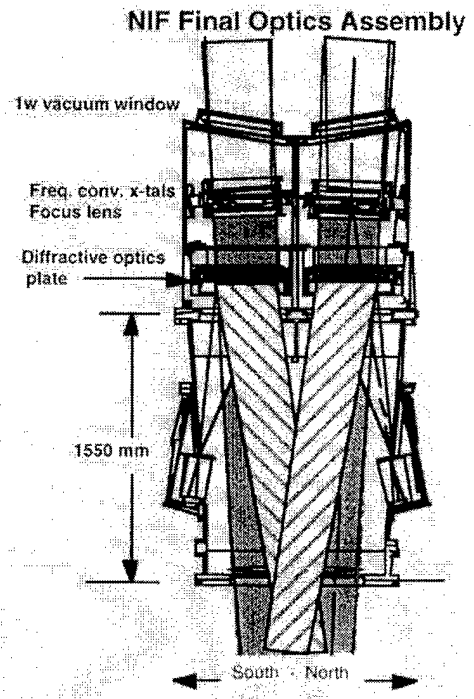

Figure 4. NIF Final Optics Assembly drawing illustrating beam crossing within a quad that will almost certainly be needed when large target arrays are fielded. The cross-hatched beams represent the crisscrossing that was accomplished by the diffractive optics plates in the cassettes that will be about 7.7 meters from target chamber center. In this configuration, the diffractive optics plates need only be long focal length "corrector lenses".

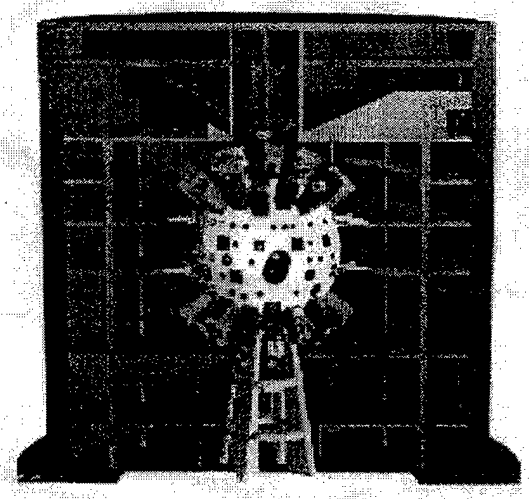

Figure 5. cutaway view of the NIF Target Area showing the 10 meter diameter aluminum target chamber. Shown is the 1.5 meter diameter radiation effects test access port on the main diagnostic level.

target chamber on its pedestal in the Target Area. The requests for the Target Area include the following items:

1. Large access port on the Target Chamber,
2. Bottom access and lift capability to handle large and heavy (up to 15 ton) fixtures ,
3. Large shield door between the Target Area and the Diagnostic Support Building,
4. Increased floor strength in the Target Area to support conceptual 'TOTIM' (Test Object Transport and Insertion Module),
5. Shielded cable trays to support data acquisition for effects testing,
6. Adequate power near the effects test port to support the TOTIM functions.

The requirements to 'not preclude' these functions in the NIF design are specified in the NIF Interface Control Document 4.1.16-1.2.2.1. This document covers all aspects of the Defense Special Weapons Agency (DSWA) Test Object Transport Inserter Module (TOTIM) experimental package WBS 4.1.16 support requirements, the assembly, installation, maintenance and support equipment requirements WBS 1.8.6.4, the LTAB facilities design WBS 1.2.2.1 and the Target Bay design WBS 1.8.4. The primary aspects covered are hoisting, transportation pathways, door openings, structural loading, and mechanical and signal interfaces in the Diagnostic Building and the Target Bay.

VI-Distributed Source Array Design

There are significant advantages in spatially dispersing individual sources to increase the fluence of source x-rays that reach the test object while maintaining test uniformity. In some test scenarios, it may also be desirable to tailor the distribution of targets around the test object to conform to the test object shape. For ±10% fluence uniformity, analysis of a simple square array with the targets at the four corners indicates an areal increase of 3.5 times over that from a simple point source of the same total energy as the array. Uniformly distributing the targets (>16) over the source and illuminating all at the same time (to maintain x-ray flux uniformity over the pulse) could further increase the test capability (10 times the uniformly illuminated area of a point source). High aspect-ratio test objects would permit even larger advantage to arrays.

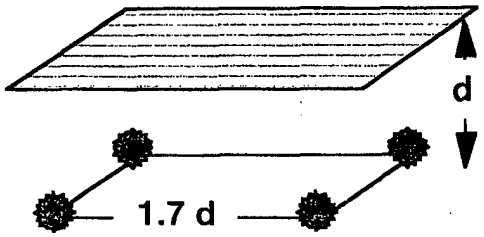

Figure 1. The area of uniform illumination of an array of sources is significantly larger than the area of uniform illumination of a point source. The area of uniform illumination (±10%) for a four-point square a factor of 3.5 times larger than for a point source with the same total energy.

However, the fielding and technology risks to implement distributed sources are greater than for point sources. The limitations due to beam geometries, unconverted light management, diffractive-optic-plate (DOP) development, and target array manufacturability are not fully known and need to be studied and/or clarified. The management of unconverted light to a target at or near the target chamber center must be considered in detail to demonstrate solutions and limitations. Clearly, the use of a diffractive optic to provide large changes in beam steering and focusing will result in a complex issue of beam targeting and source placement and the status of the ongoing distributed source array design effort will be summarized.

VI-1. Design objectives

Beam steering will be complicated with large arrays as some laser beams (or unconverted light) may be occluded by the test object, or illuminate the source support structure. Also, the unconverted light from any beamline could potentially illuminate the laser optics of another beamline causing damage. It has also been noted that large beam steering (to sources as much as ±25cm from the target chamber center would clip some of the beams at the Final Optical Assembly port. Initial beam layout drawings with a ±25cm target array indicates that some quads would have about 10% of one beam occluded. This laser power loss is considered acceptable as the increase in test capability with beam steering negates this loss. To 'not preclude' beam steering to ±25 cm and to prevent laser damage and scattered light problems from the laser hitting inside the FOA, the NIF Project has included an operator controlled aperture in the PAM It should also be noted that in the present design of the target insertion module, that there is clearance for only up to a 50 cm diameter rigid distributed source array.

On the basis of previous work on distributed arrays, the status of the NIF design and the desired test environments, simple guidelines for the initial design of distributed sources can be developed. These are the following:

1) consider baseline size of a ±25cm target array,
2) due to target dynamics, power density requirements, the number of individual targets will be 12-24,
3) 12, 16, or 24 individual targets implies 4,3 or 2 quads/targets
4) temporal stretching of x-ray pulses may be achieved by sequential delays in driving closely-spaced multiple sources at roughly the same location in the array,
5) individual targets may require a minimum spacing of order 1 cm to eliminate fratricide effects,
6) light weight, low-Z support structure will be needed to minimize debris,
7) if at all possible, design special optics to accommodate multiple source arrays.

VI-2. X-ray Source Laser Energy, Power & Targeting Requirements

The primary candidates for x-ray sources in the 3-15 keV range are underdense radiators due to their high efficiency. However, for $h\nu$ < 3-5 keV, discs sources will also be considered. Our understanding of discs and/or underdense targets can be used to develop guidelines for target focusing, power, target sizes and numbers of targets. Estimates of the laser parameters to targets will be based on the nominal NIF operation at 500 TW power for 3ω to target with a best focus of 500 micron spot size. Therefore, each quad would deliver about 10 TW of laser power. At nominal power and 500 micron spot, the incident laser intensity of a single beam would be 1.3×10^{15} watts/cm^2 and a quad would be about 5.2×10^{15} watts/cm^2.

Although useful individual x-ray source capability has already been demonstrated by Nova experiments and Lasnex modeling, the design of laser-driven x-ray sources is the subject of active research. Any detailed values of laser-drive parameters and source definition are subject to reevaluation.

It is assumed that these sources require a minimum incident laser intensity to develop the hot plasma conditions and a minimum power density requirement to maintain the emitting plasma volume. Our current best estimates of discs and/or underdense targets implies optimization of the x-ray output in the region of 1-5 keV with beam intensities of approximately 5×10^{14} watts/cm^2 and power densities of about 10^{15} watts/cm^3. For the production of 5-15 keV X-ray sources, the power and energy deposition requirements to produce efficient sources are approximately an order of magnitude larger than for sources emitting between 1-5 keV. The laser beam intensity requirement is approximately 5×10^{15} watts/cm^2 and the power density requirement is approximately 10^{16} watts/cm^3.

Assumption of the required incident beam intensity and the laser parameters allows estimates of the spot size requirements. The required plasma power density and the choice of 2, 3 or 4 quads per target determines the possible number of targets and an estimate of the target diameter. These results are shown in Table 1. For sources emitting in 1-5 keV, an individual laser beam (one of a quad) at a spot size of 810 microns is needed. Thus, each beam of a quad needs to be targeted separately from other beams. This is not the case for higher photon energy sources. The 5-15 keV sources require all four beams of a quad coincident onto the target to produce the currently-required beam intensity.

X-ray Source (keV)	Beam Intensity (W/cm^2)	Power Density W/cm^3	Spot Size* (μm)	Power/ Target (TW)	# of Targets	Target Diameter (mm)
1-5	$5x10^{14}$	~10^{15}	810/beam	10.4 (1 quad) 20.8 (2 quads) 31.2 (3 quads)	48 24 16	2.76 3.5 4.0
5-15	$5x10^{15}$	~10^{16}	515/quad	31.2 (3 quads) 41.6 (4 quads)	16 12	1.87 2.04
> 25	$5x10^{15}$		515/quad	31.2 (3 quads)	16	~2-4

*Converging focus onto target is desirable.

Table 1: Ballpark Estimates of Laser Plasma Radiation Source Parameters

1. Sources with photon energies 1-5 keV

From these general assumptions for source parameters, laser aiming, focusing & firing sequence requirements can be developed. Note that the NIF laser of 192 laser beams or 48 quads enter the target chamber in quasi-spherical symmetry. The target array is in general a plane array, thus the symmetry leads to possible targeting solutions with the number of targets to be the number of beams or quads divisible by four; *i.e.* 48, 24, 16, 12, or 8. As can be seen from Table 1, for 1-5 keV sources, the required power density can be met with 1, 2 or 3 quads (4, 8 or 12 beams) to a target, implying the possibility of 48, 24 or 16 targets, respectively. Consider the case of 20.8 TW per target, which would have 24 targets. Assuming NIF 3ω laser operation at 1.8 MJ, then each target will have 8 individual beams incident each with a spot size of order 810 microns to get the required beam intensity of $5x10^{14}$ watts/cm^2.

Different target designs will lead to different targeting limitations. Four types of targets for the 1-5 keV range are presently envisioned. These are discs, gas/plasma filled low-Z cans, gas-bags, or gas/plasma plumes. The targeting of gas-filled low-Z cans is restricted by the limitations of the number and location of laser entrance holes and the desire to volumetrically pump the plasma.

Two quads per target would imply the possibility of 24 targets with about 75 kJ per target. A possible targeting sequence would be four targets being illuminated at one time, with the successive targets being illuminated in groups of four at time intervals of equal to the individual source x-ray pulse width. Thus, for 24 targets, there could be up to 6 firing sequences that would give an effective X-ray pulse width of greater than 18-22 ns (assuming 3-4 ns/target). This assumes that all beams from a quad illuminate a target or targets at the same time. For the case of 3 Quads/target implies there can be 16 targets and the energy per target is 112.5 kJ. This gives the possibility of 4 targets per firing sequence, for a total of 4 firing sequences and a potential X-ray pulse width around 12-14 ns.

2. Sources with photon energies 5-15 keV

As can be seen from Table 1, for 5-15 keV sources, the nominally-required power density can be met with 3 or 4 quads to a target, implying the possibility of 16 or 12 targets,

respectively (@ 1.8 MJ, 3ω, 3.6 ns pulse width) which is 112.5 - 150 kJ/target. Consider the case of 41.6 TW per target with 12 targets. The projected targeting for 5-15 keV is different than for 24 targets with the 1-5 keV sources discussed above. To meet the beam intensity requirements implies all four beams of a quad are coincident onto each target, then each target will have 2 or 3 targeting locations with a spot size of order 515 microns to be subjected to the required beam intensity of $5x10^{15}$ watts/cm^2.

Again, different target designs will lead to different targeting limitations. Three types of targets for the 5-15 keV range are envisioned; gas/plasma filled low-Z cans, gas-bags, or gas/plasma plumes. The targeting of gas/plasma filled low-Z cans is much less restricted than for the lower energy sources as the number of LEHs required is 2 or 3. For all of the targets there is the desire for uniform volume excitation.

3. Greater than 25 keV Sources

For the purposes of this discussion, it will be assumed that non-ignition sources producing photons of energy >25 keV will require 1ω to targets. It is assumed in Table 1 that the required incident beam intensity is $5x10^{15}$ watts/cm^2. As with 5-15 keV sources, to meet this required beam intensity implies all four beams of a quad are co-incident onto each target (4 MJ, 8 ns pulse width), then each target will have 2 or 3 targeting locations with a spot size of order 515 microns. These targets will be similar to standard hohlraums with high-Z walls to enhance bremsstrahlung output.

VI-3. Array Design Status

The design status of potential target arrays for weapons effects testing is in its infancy. The design objectives at this point are the identification of sample array designs from estimates of target sizes and beam focusing requirements. Key to the implementation of distributed sources is the development of techniques to determine targeting scenarios with which to ensure that the laser energy can illuminate the test object, and that the energy (to include the unconverted light) does not illuminate the test object, the source support structure, or laser optics of other beams. These techniques and design tools to develop and analyze possible target array configurations are under development.

Four possible distributed array configurations are being considered. These are:
a) 24 evenly spaced targets in approximately a square;
b) targets evenly spaced over a 1 meter x 0.3 meter triangular test object;
c) 3,4 or 6 targets grouped in four evenly spaced corners to permit extending the duration of the total x-ray pulse to multiples of the duration of a single pulse, or;
d) 12-24 targets evenly spaced in a circle over the test object.

To exercise our design capabilities, we have settled first on array c) in this list. This array is illustrated in figure 2. It was noted that in the current NIF design requirements it specifies 'not to preclude' ±25 cm targets. Some test objects may require larger beam steering and focusing. Also it should be noted that the limits of operator controlled beam steering and focusing will be about ±3-5 cm. The limits of operator control will impact the number and type of optics needed. It is of interest to develop diffractive optic sets that will maintain maximum flexibility (for different distributed source geometries). More complex array geometries such as the large RV shape will be explored following the successful design of the simple array and the exercise of the design tool suite.

As discussed above, targeting requirements allows consideration of 2, 3 or 4 Quads incident on a single component of a target array. For each of the different configurations, the nominal target spacing can be specified. Targeting array elements far from target chamber center may require crisscrossing beams within a quad. In normal operations, they would be directed at the same point. This introduces additional operational challenges .

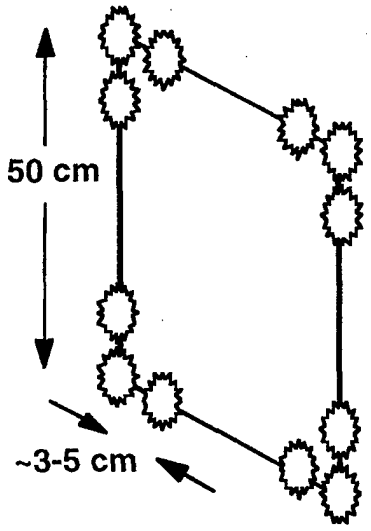

Figure 2. Preliminary target array for which we are going through the exercise of integrating into the NIF target chamber. It is this target array that we will use to test the software and the procedures that we are developing.

We began constructing a software modeling tool for analyzing the distribution of the laser light inside the NIF target chamber from the viewpoint of NWET applications. Our software package is being written in the IDL language and relies heavily on the package being developed for the light analysis for the normal NIF operation Although there are conceptual similarities in the two cases, there are many significant differences. Some of these are: a) use of the color separation grating (CSG) as opposed to the Fresnel lens for redistributing the laser light, b) large focal spot offsets (up to ~ 1m) in the NWET case as compared to relatively small (~3-5 cm primarily for backlighting) in the ICF and Weapons Physics cases. The distribution of focal spots in the case of an off-axis Fresnel lens combined with the main focus lens (NWET) is very different from the distribution of the focal spots for a CSG combined with the focus lens. This necessitates a significant modification to the unconverted light modeling and visualization (ULMV) package being developed for ICF configurations of NIF. We have begun the construction of a modified software package for analyzing the light distribution in the NWET configurations. This package will help us analyze the distribution of the focal spots in the target chamber center and also the distribution of the unconverted light at the opposite chamber wall. We will be able to answer questions like - is the light entering an opposing port? - is the light clearing the Final Optics Assembly, the target assembly and the test object? This work is essential to develop a diffractive optic design for the full 192 beam system that will achieve the required focal spot distribution for the NWET experimental configurations.

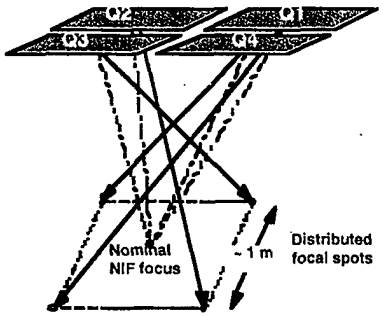

Figure 3. With beam crisscrossing within a given quad (set of four beams) , focal spots shifts of approximately 80 cm are possible with the current Final Optics Assembly (FOA) configuration.

VI-4. Diffractive Optics / Fresnel Lens Development

The software development effort is complemented with an optical engineering analysis of the assessment of the Fresnel lens requirements for moving the focal spots by distances approaching 1 meter. Preliminary assessment indicates that the required Fresnel lens focal lengths are in the range of 200-500 m. We have begun an assessment of the technology development required for fabrication of the NWET Fresnel corrector lenses.

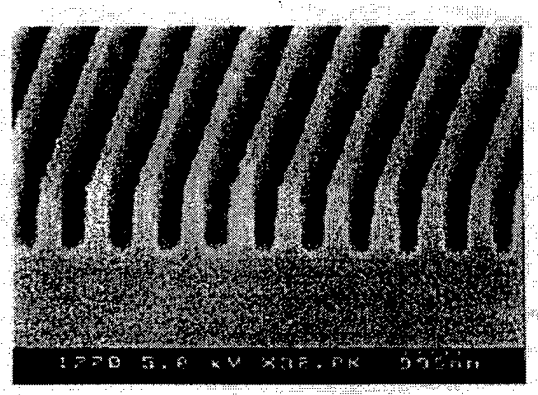

Figure 4. Example of a high-efficiency grating etched in fused silica The grating period of this sample is 350 nm and the grating depth is 600 nm

In addition to the optical analysis of the Fresnel lens requirements, we also conducted a preliminary evaluation of whether it is feasible to distribute the focal spots over a meter area near the target chamber center. It is possible to move the focal spots over a meter if one 'crisscrosses' the four beams within a quad. A more detailed analysis with a specific layout will be carried out once the software package is developed

The best Fresnel lenses fabricated so far are about 2-cm in diameter and have 92% focusing efficiency. It is in our estimation that significant technology development is required to fabricate corrector Fresnel lenses for effects test applications. To achieve high efficiency, the phase profile within each zone has to be fabricated either as a continuous blaze or as a discretized structure with at least 16 levels within each zone. LLNL is beginning a technology development program for fabrication large aperture corrector Fresnel lenses for use on the NIF. Their experience with fabrication large area diffractive optics (kinoform phase plates for Nova (65 cm diameter) and Beamlet (56 cm diagonal)) should enable them to develop the technology to successfully fabricate such lenses for use on the NIF.

The technology development program consists of first demonstrating a 16-level Fresnel lens in fused silica at about 6" diameter using four binary masks and wet etching. Following this demonstration, the technology would need to be scaled-up for fabricating a full-aperture Fresnel lens in FY99. In parallel to this development effort, there is the task of developing distributed source layout designs. Based on the actual focal lengths and offsets needed for potential distributed source designs, a set of Fresnel lenses would be fabricated for fielding on the NIF at the time of the first bundle activation.

VII-NIF Construction, Startup, and NRSUG Plans

VII-1. Construction

Construction at the NIF site began in the middle of 1997. There were a several curve balls served up by fate: 1) the unearthing of some old, undocumented, buried capacitors, 2) finding mammoth bones late in the year that turned part of the NIF site into an archeological excavation, and 3) the non-stop El Nino rains that led to the hiring of a construction consultant firm from Seattle to learn how to work under such conditions. Amazingly enough, there was only a minor perturbation to the overall schedule. The site as it looked at the depths of the excavation in April 1998 is shown in the aerial photograph shown in fig. 1.

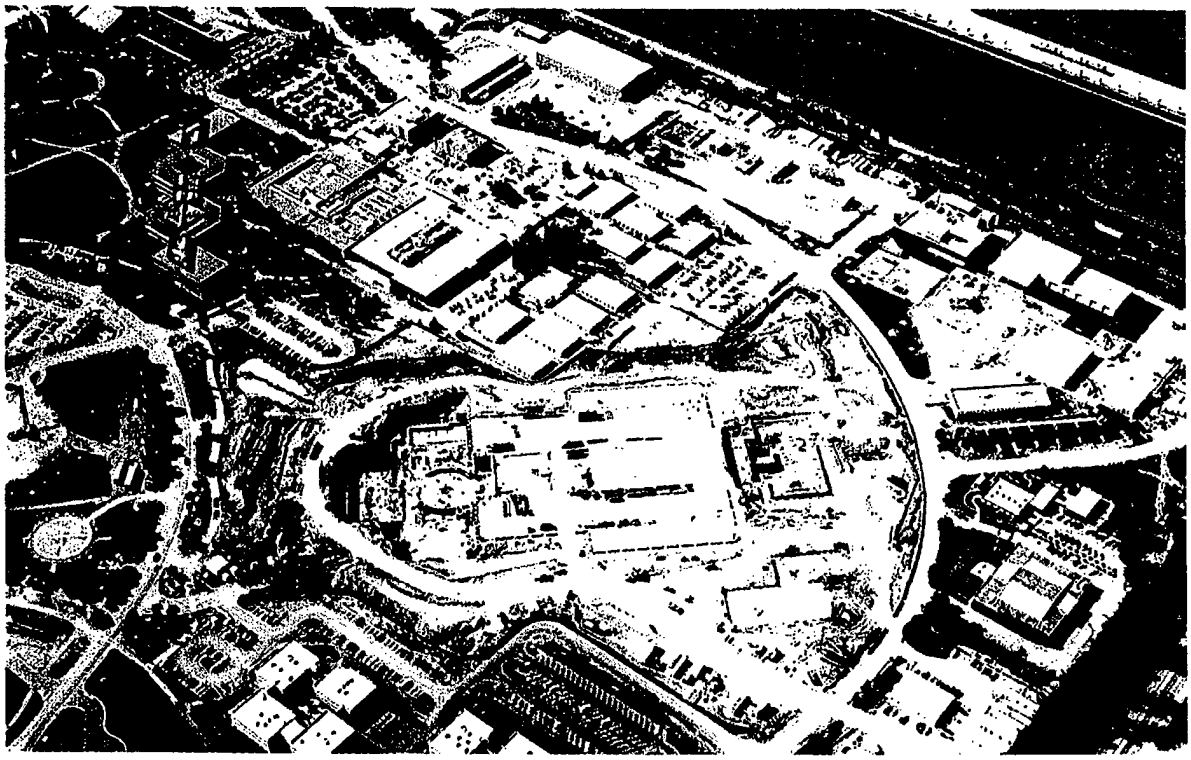

Figure 1. The NIF construction site on April 20, 1998

VII-2. Startup

The NIF will be built and activated in stages. It is designed as a modular 192 laser-beam facility. There are two laser bays as shown in figure 2. One set of eight beams (two quads) will initially be activated as indicated. At full power, these two quads will provide approximately twice the energy in blue light as does Nova and will give all experimentalists

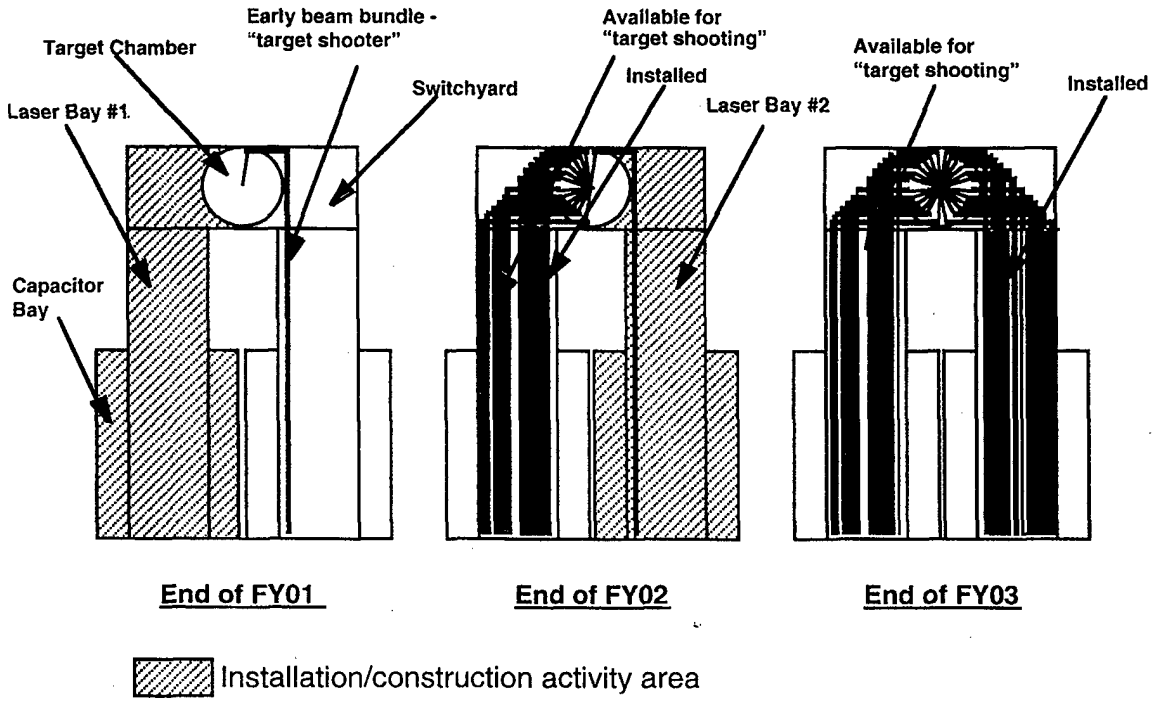

Figure 2. NIF's modular design permits initial experiments to be performed early in the construction.

an opportunity to continue work at LLNL and to learn how to use NIF (it will be very different from Nova from an operational standpoint). Construction of additional beams will proceed in the other laser bay. Following construction and checkout of the new constructed beam bundles, they will be made available to experiments at a rate that is plotted in figure 3. This shows the projected available laser energy as a function of time. The NIF Project will be complete when all laser beams will have been installed. Qualification of the last laser beams will then be the responsibility of NIF Operations and not the Project.

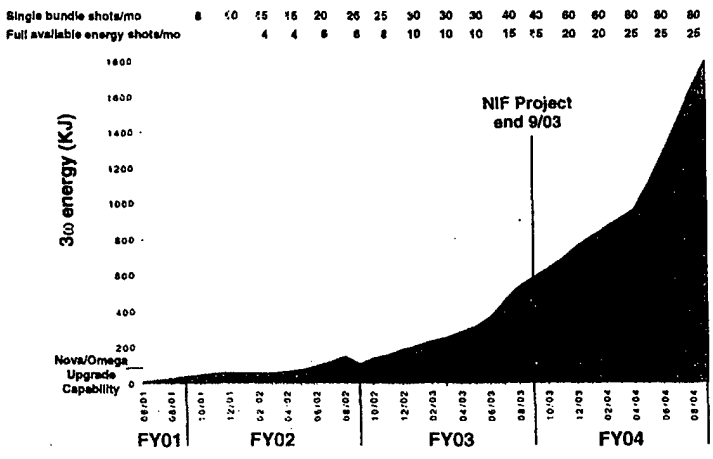

Figure 3. Plot of projected available NIF energy vs. time from startup to full power.

VII-3. Plans

The radiation effects testing community through the NIF

Radiation Sciences Users Group (NRSUG) has been working with the Defense Special Weapons Agency to formulate a plan to serve as a guide for future funding needs and to present to the NIF Project and DOE as the milestones that need to be met on the way to providing a meaningful radiation effects testing capability at the National Ignition Facility. This plan has been briefed to and approved by the highest administrative levels within the DSWA in late 1997. It is anticipated that the radiation effects testing community will be using 7.5% of NIF shots per year commencing with the first bundle of NIF.

#	Goal	Testable Objects	Suggested Intermediate Demonstration Goal
I Clean Cold	FY05, 1-2 keV Blackbody (equiv.) ~1 cal/cm^2 - 3,000 cm^2, *Clean*, ± 10% uniformity	Optical Components, Assemblies	1,000 cal 1 cal/cm^2, 1,000 cm^2
II High Fluence Cold	FY05, 1-2 keV Blackbody (equiv.) >20 cal/cm^2 - 2,000 cm^2, ± 10% uniformity,	Strategic Materials	2,000 cal >20 cal/cm^2, 100 cm^2
III Medium Fluence Cool	FY06, 3-4 keV Blackbody (equiv.) 5 cal/cm^2 - 1,000 cm^2 ± 10% uniformity	Strategic Materials, Structures	250 cal 5 cal/cm^2, 50 cm^2
IV Hot	FY04, 15-20 keV Blackbody (equiv.) 20 krads(Si) - 10,000 cm^2 < 10 ns pulsewidth	Electronic for interceptors and RVs	1 krad(Si), 1,000 cm^2
V Ignition: Warm-to-hot	FY09, 10 keV Blackbody (equiv.) with Ignition >1 MJ >10 keV 100 krads(Si) - 10,000 cm^2	Strategic Materials, Strructures, Components	10 MJ yield from SLIC seeded capsule

Table 1. NRSUG-DSWA defined radiation effects testing goals for NIF. This is the status of the goals at the end of 1997.

The required research, development and engineering activities are extensive. Some are of common interest with other potential NIF users, others are unique to this community. The draft plan for NWET activities until the completion of NIF are presented in table 2 on the next page. These plans will continue to evolve as more information about NIF operation is developed.

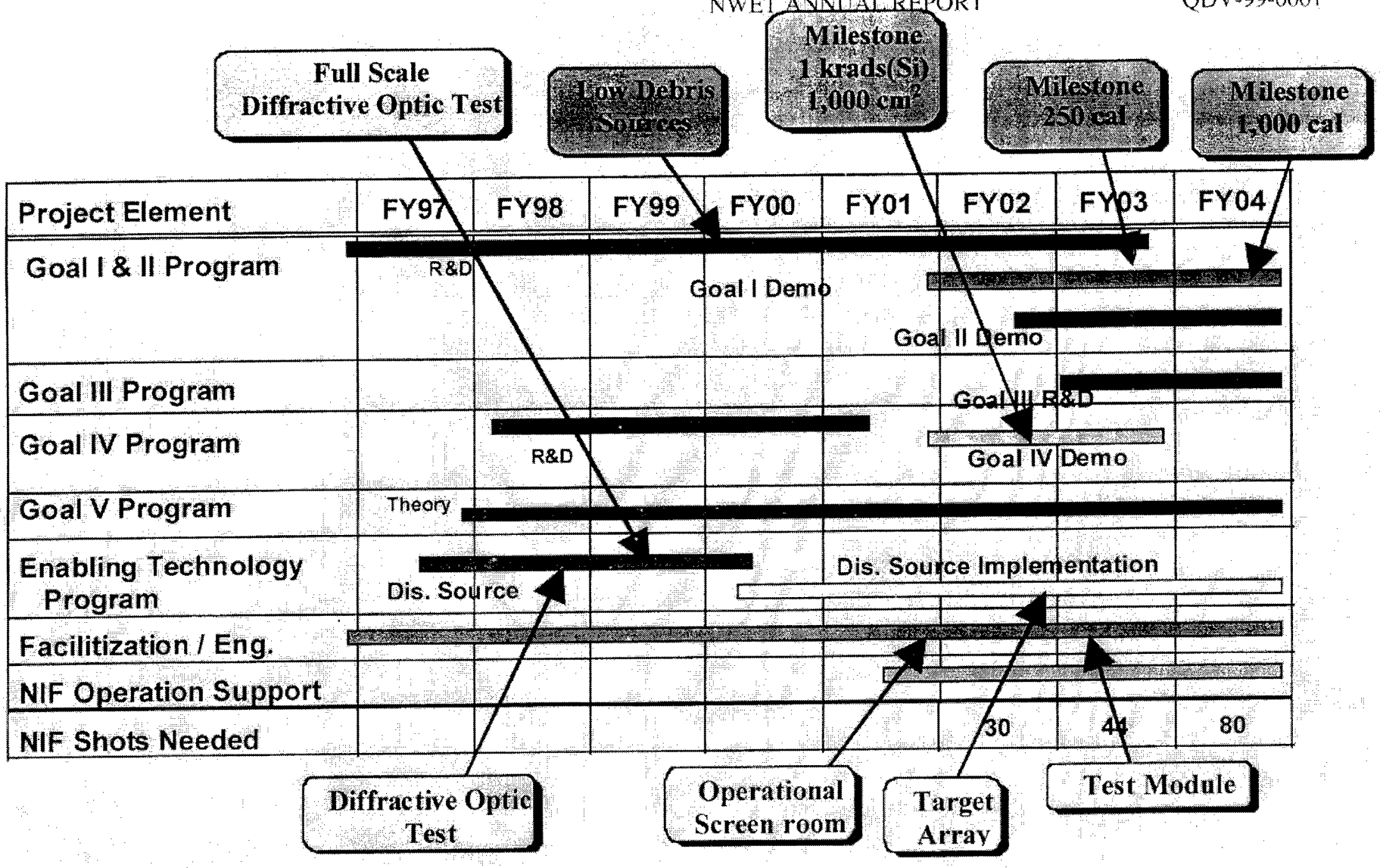

Table 2 Proposed Test Demonstration Plan

VIII-Non-Ignition X-ray Source Fluence-Area Products for Nuclear Weapons Effects Testing on NIF

VIII-1. Introduction

A major feature of the National Ignition Facility is that its 192 beams can drive arrays of laser-driven x-ray sources. The ability to allow beam steering up to 50 cm away from target-chamber center has not been precluded in the NIF design. Indeed, a multidisciplinary team of physicists and engineers supported by DSWA has been studying the issues surrounding facilitization of such target arrays at NIF starting in late FY97. It is of interest to update projections of the capabilities of these target arrays. The fluence-area product of an array will depend on a number of factors such as the total energy available to drive the targets, the efficiency of the laser-driven production of x-rays, the attenuation of debris mitigation and the solid angle subtended with the required uniformity of fluence.

The fluence-area product for NIF can be expressed

$$F \times A = E_{NIF} \times \mu \times T \times \Delta\Omega$$

where E_{NIF} is the NIF energy that can be coupled to the sources, μ is the source efficiency per steradian (source efficiency/solid angle), T is the debris shield transmission and $\Delta\Omega$ is the solid angle that can be collected from an individual source and still have the requisite uniformity (for purposes of this discussion, we will use $\pm 10\%$).

VIII-2. Components of the Fluence x Area Product Formula

1. Usable NIF energy, E_{NIF}:

NIF's usable energy depends on the target type and pulse length. If the targets are thick slabs, then we assume that only 1/2 of NIF will be usable since x rays produced by the other half of NIF would be seen by the test object. With underdense sources, which are more like isotropic sources, we assume that all NIF beams might be used.

The usable energy also depends on the pulse shape. In previous estimates we always assumed that NIF is a 1.8 MJ, 500-600 TW laser, producing a pulse length of ~3 ns. Figure 1 is a more recent, better estimate of NIF energy vs. pulse length (ref. 1). The performance ranges from 0.85 MJ in 1 ns to 2 MJ in 3 ns to over 3 MJ in 10 ns. These latest estimates of NIF fluence area products consider this performance.

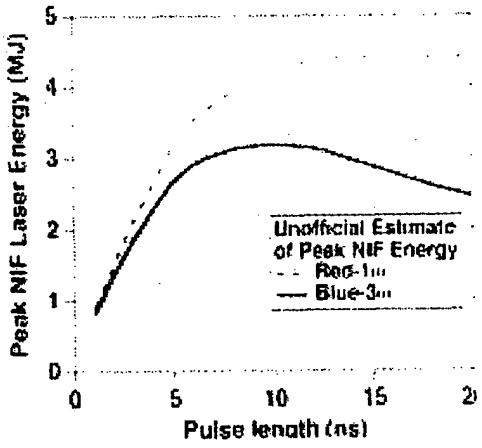

Figure 1. Unofficial, 1996 estimate of NIF energy vs. pulse duration for red and blue light (ref. 1).

2. Source efficiency per steradian, μ:

In projecting NIF fluence-area products we consider three types of sources: demonstrated discs, demonstrated gas bags and predicted NIF sources. The demonstrated discs and gas bags are from NOVA experiments and are described in ref. 2 (see appendix). There are four demonstrated sources of interest:

1) Au disc radiating 0-1 keV photons. The total conversion efficiency is ~70%. The radiation from the disc goes into approximately 2π steradians, so μ_{disc} is ~11%/sr.
2) Au disc producing M-band radiation (2-3 keV) at ~15% efficiency. This is a 2π source, so μ~2.4%/sr.
3) Xe-gas-bag M-shell radiation (1-2 keV). Approximately 25% efficiency into 4π. For this source μ ~2%/sr .
4) Xe-gas bag L-shell radiation. (4-7 keV); ~8% efficiency into 4π. μ~0.6%/sr. All these measurements were made on targets irradiated with 1 ns pulses.

Predicted multi-keV source efficiencies for NIF come from 2-D LASNEX modeling. As described in ref. 4, 2D design of NIF multi-keV sources has focused on two types of underdense sources; gas columns and tamped sources (Be cans filled with a low density mid-Z material). Because a gas column is, by definition, heated by only one of NIF's beams, it is restricted to ~10 TW maximum power. Tamped sources remove this power restriction since they allow several beams to be fired into a target. Tamped source designs exist up to 60 TW.

Xenon gas columns have been modeled with 2 and 3 ns pulses. Our 3 ns simulations indicate that about 18% of the laser energy will be converted into L-shell radiation (>4 keV) and about 45% into M-shell emission (1-2 keV) and 65% into radiation at all energies. We have also modeled gas columns of other materials (such as Fe and Ge) which produce higher photon energy radiation. This work shows that at higher photon energies, gas columns are not as efficient as tamped sources, at least for pulse lengths of 2 ns. Moreover, since tamped sources are amenable to NOVA experiments, our design work on column sources has been limited.

With the tamped source we have investigated a wide variety of source materials. We have evaluated these sources at power levels between 20 and 60 TW; well within NIF's 500-750 TW capabilities. This design work has been done only for pulse lengths of 2 ns. (Longer pulse design work has been deferred in favor of supporting NOVA proof-of-principle experiments that are 2 ns duration.)

Our predicted performance for the tamped sources in summarized in table 1 below:

element	Laser power	fraction of laser energy > *hv* (keV)	
Kr	60 TW	4%>13 keV	30%>2 keV
Ge	60 TW	14%>10	26%>2
Ge	50 TW	10%>10	26%>2
Ge	30 TW	7%>10	20%>2
Cu	40 TW	11%>8.5	26%>2
Cu	30 TW	10%>8.5	24%>2
Dy	60 TW	9%>8	24%>2
Xe	60 TW	30%>4	48%>1
Xe	50 TW	26%>4	48%>1
Xe	30 TW	22%>4	40%>1
Xe	20 TW	17%>4	37%>1

Table 1. Predicted performance for tamped-source targets taken from ref. 4. These targets are approximately isotropic sources. The source efficiency per steradian, μ, is found by dividing the above efficiencies by 4_.

3. Debris shield transmission, T:

For this work we assume no debris shield attenuation. For photons >4 keV, this should be a fair assumption. At lower photon energies, it is incorrect.

4. Solid angle, ΔΩ for ±10% uniformity:

A constraint of ±10% uniformity on the experimental object limits the solid angle we can usefully collect from each source. For an isotropic point source this solid angle is 0.45 sr. For four, appropriately distributed isotropic sources, the solid angle we can utilize from each source rises to 1.6 sr. For 25 appropriately distributed, isotropic sources it is 4.5 sr. In the limit of an infinite number of isotropic point sources distributed on a plane, the solid angle would be 2π sr.

VIII-3. Estimated Fluence x Area products:

Table 2 lists fluence area products (in calories) using experimentally demonstrated efficiencies and various fielding, pulse length scenarios. The upper part of this table is the most conservative estimate we can make, assuming 1 ns pulse length as was used on the NOVA experiments. This is a "guaranteed" minimum performance. Sections of this table list performance assuming targets irradiated at 2, 3 and 6 ns have the same efficiency as those irradiated at 1 ns. Assuming this to be true to 3 ns is probably reasonable; assuming it to be true at 6 ns is somewhat speculative. Thus, using demonstrated-on-NOVA efficiencies and a large number of sources, we project, with reasonable confidence, fluence area products of ~90,000-120,000 calories in the 0-1 keV range; 32,000-43,000 calories in the 1-2 keV range; 19,000-26,000 calories in the 2-3 keV range; and 10,000-13,000 calories in the 4-7 keV range. More speculative are the 6 ns estimates of ~180,000 calories, 64,000 calories, 39,000 calories and 19,000 calories in the same spectral ranges.

Table 3 lists fluence area products (in calories) using efficiencies found in 2D LASNEX design simulations of tamped targets. The single point and four point sources assumed that at least 60 TW per source would be available. The 25-point source column assumed 20-30 TW per source would be available (The NIF of ref. 1 can drive 25 sources at 30 TW/source for 2 ns; 27 TW/source for 3 ns; 20 TW/source for 6 ns).

The upper section of table 3 assumes the sources will only work for 2 ns. The central section of table 3 assumes that sources can be designed for 3 ns that have the same efficiency as the 2 ns sources. This is probably a fair assumption. The lower part of table 3 assumes that sources can be designed for 6 ns pulses that have the same efficiency as the 2 ns sources. This is speculative.

Table 3 suggests that we can reasonably hope to have sizable fluence area products in the multi-keV regime. Up to ~38,000 calories in 4-7 keV; ~12,000 calories around 10 keV; dropping to ~2400 calories at 13 keV. More speculative are the 6 ns predictions of ~44,000 calories, 18,000 calories and 3600 calories in the same spectral regions.

Table 4 shows the projected performance from arrays of Xe gas columns irradiated with ~10 TW single NIF beams. Targets such as these may lead to fluence area products of ~30,000 to 45,000 calories in the 4-7 keV range and 77,000 to 116,000 calories in the 1-2 keV range.

VIII-4. References

1. J. Hunt, J. Auerback, S. Haney, "Unofficial estimate of the UV power and Energy that NIF can deliver to a target", LLNL-NIF-96-427 (May, 1996).
2. R. L. Kauffman, L. J. Suter, H. N. Kornblum, D. S. Montgomery, "X-Ray Production in Laser-Heated Xe Gas Targets", ICF Quarterly Report, January-March 1996, LLNL, UCRL-LR-105821-96-2, p 43.
3. R. Kauffman, *Handbook of Plasma Physics; Vol. 3 Physics of Laser Plasmas*, Eds., A. M. Rubenchik and S. Witkowski (North Holland, Amsterdam 1991), p. 123.
4. L. J. Suter, R. L. Kauffman, M. S. Maxon, J. F. Davis, "Efficient Production and Applications of 2- to 10-keV X Rays by Laser-Heated 'Underdense Radiators'", ICF Quarterly Report, April-June 1996, LLNL, UCRL-LR-105821-96-3, p 96.

FxA products using experimentally demonstrated efficiencies

Assuming the 1ns pulse length used in the Nova experiments

souce	hv range	eff/sr	Usable NIF MJ	1pt (cal)	4pt (cal)	25pt (cal)
Au disc	0-1keV	0.11	0.425	5033	17895	50329
Xe bag M	1-2keV	0.02	0.85	1830	6507	18301
Au disc M	2-3keV	0.024	0.425	1098	3904	10981
Xe bag L	4-7keV	0.006	0.85	549	1952	5490

Assuming targets have the same efficiency at a 2ns pulse length

souce	hv range	eff/sr	Usable NIF MJ	1pt (cal)	4pt (cal)	25pt (cal)
Au disc	0-1keV	0.11	0.75	8882	31579	88816
Xe bag M	1-2keV	0.02	1.5	3230	11483	32297
Au disc M	2-3keV	0.024	0.75	1938	6890	19378
Xe bag L	4-7keV	0.006	1.5	969	3445	9689

Assuming targets have the same efficiency at a 3ns pulse length

souce	hv range	eff/sr	Usable NIF MJ	1pt (cal)	4pt (cal)	25pt (cal)
Au disc	0-1keV	0.11	1	11842	42105	118421
Xe bag M	1-2keV	0.02	2	4306	15311	43062
Au disc M	2-3keV	0.024	1	2584	9187	25837
Xe bag L	4-7keV	0.006	2	1292	4593	12919

Assuming targets have the same efficiency at a 6ns pulse length

souce	hv range	eff/sr	Usable NIF MJ	1pt (cal)	4pt (cal)	25pt (cal)
Au disc	0-1keV	0.11	1.5	17763	63158	177632
Xe bag M	1-2keV	0.02	3	6459	22967	64593
Au disc M	2-3keV	0.024	1.5	3876	13780	38756
Xe bag L	4-7keV	0.006	3	1938	6890	19378

Table 2. Predicted NIF Fluence-Area products for various pulse durations using experimentally measured efficiencies for conversion of laser light to x rays.

Projected NIF FxA products using 2D Lasnex efficiencies

Be tamped mid Z filled targets

Assume 2ns source and 2ns efficiencies

source	hv range	eff per steradian at 60TW	eff per steradian at 30TW	Usable NIF MJ	1pt (cal)	4pt (cal)	25pt (cal
tamped Xe	>1keV	0.038	0.0318	1.5	6136	21818	51352
tamped Xe L	4-7keV	0.024	0.0175	1.5	3876	13780	28260
tamped Dy	>2keV	0.0191		1.5	3084	10967	
tamped Dy L	~8keV	0.0071		1.5	1147	4077	
tamped Cu	>2keV	0.0207	0.0191	1.5	3343	11885	30843
tamped Cu K	~9keV	0.0088	0.008	1.5	1413	5024	12919
tamped Ge	>2keV	0.0207	0.016	1.5	3343	11885	25837
tamped Ge K	~10keV	0.0111	0.0056	1.5	1792	6373	9043
tamped Kr	>2keV	0.024		1.5	3876	13780	
tamped Kr L	~13keV	0.0032		1.5	514	1826	

Assume 3ns source with 2ns efficiencies

source	hv range	eff per steradian at 60TW	eff per steradian at 30TW	Usable NIF MJ	1pt (cal)	4pt (cal)	25pt (cal
tamped Xe	>1keV	0.038	0.0318	2	8182	29091	68469
tamped Xe L	4-7keV	0.024	0.0175	2	5167	18373	37679
tamped Dy	>2keV	0.0191		2	4112	14622	
tamped Dy L	~8eV	0.0071		2	1529	5435	
tamped Cu	>2keV	0.0207	0.0191	2	4457	15847	41124
tamped Cu K	~9keV	0.0088	0.008	2	1884	6699	17225
tamped Ge	>2keV	0.0207	0.016	2	4457	15847	34450
tamped Ge K	~10keV	0.0111	0.0056	2	2390	8498	12057
tamped Kr	>2keV	0.024		2	5167	18373	
tamped Kr L	~13keV	0.0032		2	685	2434	

Assume 6ns source with 2ns efficiencies

source	hv range	eff per steradian at 60TW	eff per steradian at 30TW	Usable NIF MJ	1pt (cal)	4pt (cal)	25pt (cal
tamped Xe	>1keV	0.038	0.0294	3	12273	43636	94952
tamped Xe L	4-7keV	0.024	0.0135	3	7751	27560	43600
tamped Dy	>2keV	0.0191		3	6169	21933	
tamped Dy L	~8eV	0.0071		3	2293	8153	
tamped Cu	>2keV	0.0207	0.0191	3	6685	23770	61687
tamped Cu K	~9keV	0.0088	0.008	3	2826	10048	25837
tamped Ge	>2keV	0.0207	0.016	3	6685	23770	51675
tamped Ge K	~10keV	0.0111	0.0056	3	3585	12746	18086
tamped Kr	>2keV	0.024		3	7751	27560	
tamped Kr L	~13keV	0.0032		3	1027	3652	

Table 3. Predicted NIF Fluence-Area products for Be-tamped sources for various pulse durations using calculated efficiencies for conversion of laser light to x rays.

Projected NIF FxA products using 2D Lasnex efficiencies

Xe gas column source

Assuming 3ns pulse and 3ns efficiencies

souce	hv range	eff/sr	Usable NIF MJ	1pt (cal)	4pt (cal)	25pt (cal)
Xe gas column	total rad	0.052	2	11196	39809	111962
Xe gas column	>1keV	0.036	2	7751	27560	77512
Xe gas column	4-7keV	0.014	2	3014	10718	30144

Assuming 6ns pulse with 3ns efficiencies

souce	hv range	eff/sr	Usable NIF MJ	1pt (cal)	4pt (cal)	25pt (cal)
Xe gas column	total rad	0.052	3	16794	59713	167943
Xe gas column	>1keV	0.036	3	11627	41340	116268
Xe gas column	4-7keV	0.014	3	4522	16077	45215

Table 4. Predicted NIF Fluence-Area products for xenon gas column sources for various pulse durations using calculated efficiencies for conversion of laser light to x rays.

UCRL-JC-133428
Preprint

Preliminary Demonstration of Power Beaming With Non-Coherent Laser Diode Arrays

Jordin T. Kare
Fred Mitlitsky
Andrew Weisberg

This paper was prepared for submittal to
Space Technology and applications International Forum (STAIF-99)
Albuquerque, NM
Jan. 31-Feb. 4, 1999

February 26, 1999

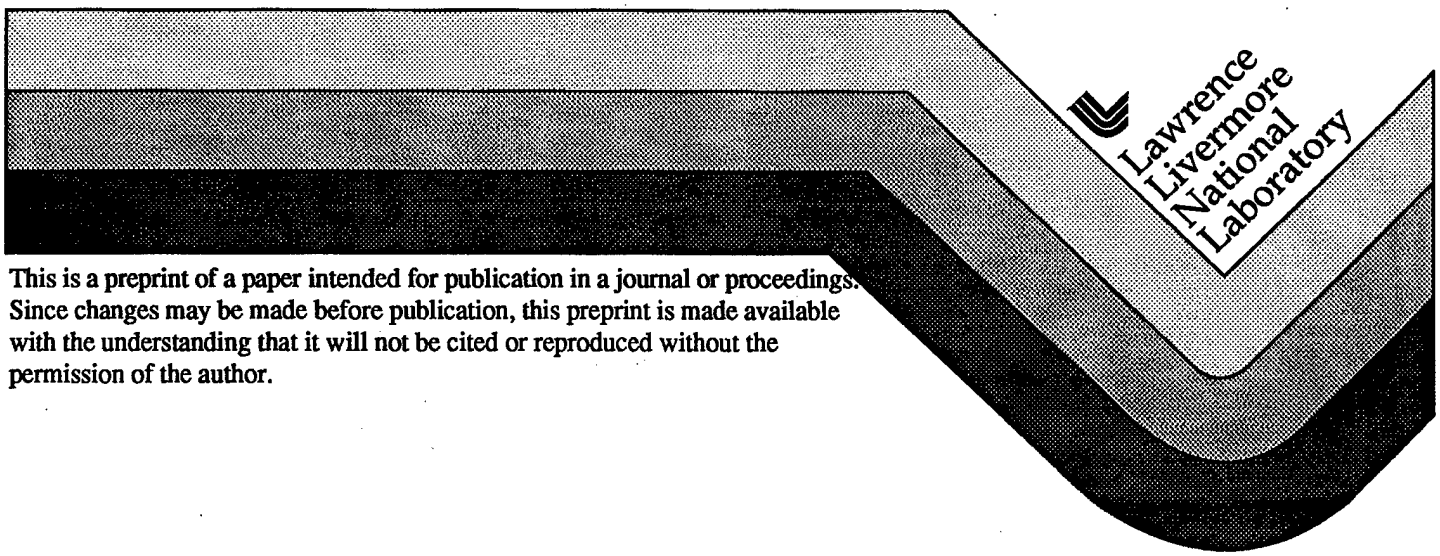

Preliminary Demonstration of Power Beaming With Non-Coherent Laser Diode Arrays

Jordin T. Kare[1], Fred Mitlitsky[2], and Andrew Weisberg[2]

[1] *Kare Technical Consulting, 222 Canyon Lakes Pl., San Ramon, CA 94583 jtkare@ibm.net*

[2] *Lawrence Livermore National Laboratory, L-174, P.O. Box 808, Livermore, CA 94551 fm@llnl.gov*

Abstract. A preliminary demonstration of free-space electric power transmission has been conducted using non-coherent laser diode arrays as the transmitter and standard silicon photovoltaic cell arrays as the receiver. The transmitter assembly used a high-power-density array of infrared laser diode bars, water cooled via integrated microchannel heat sinks and focused by cylindrical microlenses. The diode array composite beam was refocused by a parabolic mirror over a 10 meter path, and received on a ~15 x 25 cm panel of thinned single crystal high efficiency silicon solar cells. The maximum cell output obtained was several watts, and the cell output was used to drive a small motor. Due to operating constraints and unexpected effects, particularly the high nonuniformity of the output beam, both the distance and total received power in this demonstration were modest. However, the existing transmitter is capable of supplying several hundred watts of light output, with a projected received electric power in excess of 200 watts. The source radiance is approximately 5 x 10^9 W/m^2-steradian. With the existing 20 cm aperture, useful power transmission over ranges to ~100 meters should be achievable with a DC to DC efficiency of greater than 10%. Non-coherent sources of this type are readily scalable to powers of tens of kilowatts, and with larger apertures can be used directly for power transmission up to several kilometers. Future non-coherent diode laser sources may be suitable for power transmission over hundreds of kilometers. Also, the experience gained with non-coherent arrays will be directly applicable to power beaming systems using coherent diode arrays or other array-type laser sources.

INTRODUCTION

Wireless power transmission by laser has been proposed repeatedly, e.g., (Landis, 1994). The primary advantage of coherent laser power transmission over microwave transmission is that the laser wavelength is much shorter, so longer ranges can be achieved with smaller transmit and receive apertures. Unfortunately, the high cost, low electrical efficiency, and limited selection of wavelengths of coherent laser sources has prevented their use in any practical application, or even realistic demonstration, of power transmission.

However, laser power transmission also has other advantages over microwaves:

- Photovoltaic receivers may already exist on the desired platform, or may be easier to incorporate than rectennas
- Optical power can be transmitted where RF cannot: in RF-sensitive environments, through small apertures (including optical fibers), through RF shields, etc.
- Optical power can be concentrated to very high power density at a receiver

If the requirement for coherence is relaxed, high-power laser diode arrays can provide arbitrary optical power at efficiencies of 40 to 50%, and wavelengths nearly ideally matched to both Si and GaAs photovoltaic cells, at comparatively low cost.

With the development of densely-packed laser diode arrays and microlens focusing (1- or 2-dimensional lenses mounted directly in front of individual laser diodes) the radiance (power per unit area per unit solid angle) available from noncoherent diode arrays has reached ~10^{11} W/m^2-sr, three to four orders of magnitude higher than non-laser sources such as high pressure arc lamps. This is sufficient for selected power beaming applications, including laser-powered experimental aircraft and power transmission between co-orbiting spacecraft. Foreseeable technical

improvements[1] can provide noncoherent radiances in excess of 10^{13} W/m^2-sr, which is sufficient for power transmission to or from low Earth orbit.

To gain an understanding of the possibilities and difficulties of non-coherent laser power transmission, the authors attempted to assemble a small, short-range power beaming system using available hardware. To our knowledge, this is the first demonstration of free-space power transmission using an noncoherent laser diode source.

LASER SOURCE

The laser source used was a microchannel-cooled diode array originally developed for diode pumping of solid state laser media. These arrays are described in detail in (Beach, 1990). The array used consisted of 25 individual "wafers"; each 0.1 x 1 x 1.5 cm wafer having a laser diode bar along one edge and a set of water cooling channels. The wafers are stacked between metal end blocks which provide both electrical contacts and water inlet and outlet connections.

The diode bars, fabricated by LLNL, produce approximately 25 watts CW, with an output divergence of, nominally, 0.1 x 1 radians (Figure 2a). The cylindrical microlens converges this beam on the "wide" axis to produce an output beam with divergence nominally 0.1 x 0.01 radians (Figure 2b).

The assembly used for this experiment was built to pump a high average power solid state laser (Comaskey, 1992) and had previously been measured to operate at up to 578 watts at an operating point of 60 A and 43.1 V, for an efficiency (DC to optical power) of 22.4% (Mitchell, 1997). Similar arrays operate at efficiencies as high as 45 - 50%. In this experiment, the source was operated from a regulated DC power supply at a maximum voltage of 44 volts and a maximum current of 35 A. At these conditions the array optical power output was measured at 243 W, as described below, for an efficiency of 16%. Power transmission tests were run at 42 volts/20 A; at these conditions the laser power output was measured at 28.6 W. The associated efficiency is 3.4%. This low efficiency is characteristic of laser diode arrays operated only slightly above their threshold current. The output wavelength was near 850 nm in the near infrared.

OPTICS

A 20 cm diameter parabolic mirror with a focal length of 1.2 m (f/6) was used to reimage the source onto the receiving array. Since in the "wide" direction of the array, its output was approximately f/10, the beam nearly filled

FIGURE 1. Laser Assembly

the mirror in one direction with the array located near the focal point. The beam illuminating the mirror was significantly narrower in the other dimension; a future experiment could use an anamorphic optic to diverge the beam in the "narrow" direction to fill (and thus efficiently use) the mirror.

---

[1] An array of single mode diffraction-limited sources has on-axis radiance P/λ^2, where P is the power of a single source. At 0.8 μm wavelength, the array radiance reaches 10^{13} W/m^2-sr when individual sources -- single mode diodes or, e.g., phase-locked subarrays -- produce greater than 6.4 watts. Combining sources with different polarizations or wavelengths can also increase radiance.

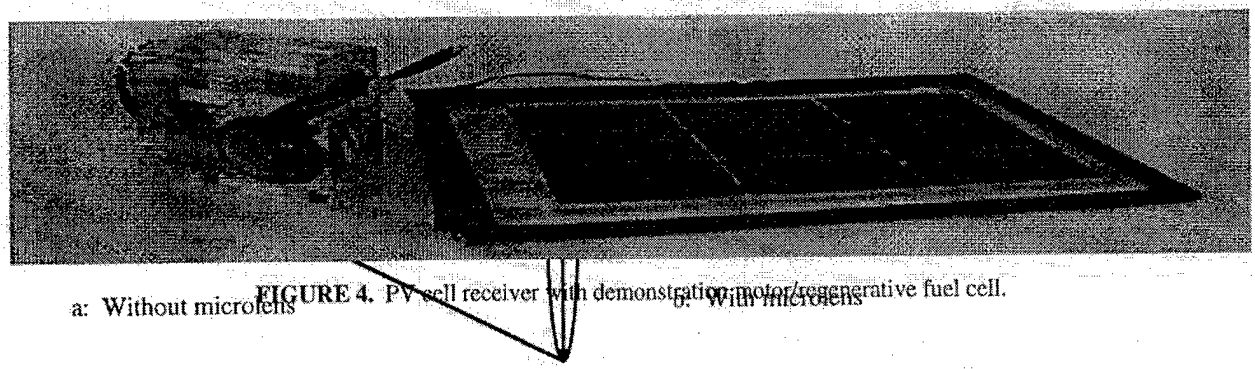

a: Without microlens b: With microlens

FIGURE 4. PV cell receiver with demonstration motor/regenerative fuel cell.

FIGURE 2. Diode array beam divergence.

A 30 cm square plane first surface mirror with a gold overcoat for high infrared reflectivity was used to bounce the beam to provide a longer beam path within the available laboratory space. The overall optical arrangement is sketched in Figure 3.

The beam profile at various points was measured using a diffuse target (white paper) and a Cohu 4915 CCD-camera. The CCD camera provides relative intensity information across the beam, which was analyzed using a BVAM101 BeamView Analyzer from Big Sky Corp.. A Coherent Labmaster power meter placed directly in the array output beam was used to measure the absolute power into a 1.8 cm diameter circular aperture, and thus calibrate the profile sensor.

RECEIVER

The receiver consisted of an array of 9 high efficiency thin film Si photovoltaic cells manufactured by Sunpower, Inc., with an active area of 3.8 x 7.9 cm. These cells were grouped in two series strings, one of 6 cells and one of 3 cells, as shown in Figure 4. These cells had an efficiency in sunlight of 18%. They were part of a lot originally intended for use in a solar-powered airplane project, which was also the source of the demonstration regenerative fuel cell used as a test load (Mitlitsky 1993). These particular cells were laminated between plastic sheets of "viewgraph protector" material (polystyrene) as part of a demonstration package, a fact which proved detrimental to the experiment. The cells were interconnected with soldered copper ribbon.

RESULTS

The transmitted beam was substantially less uniform than had been hoped. A sample beam profile at the receiver

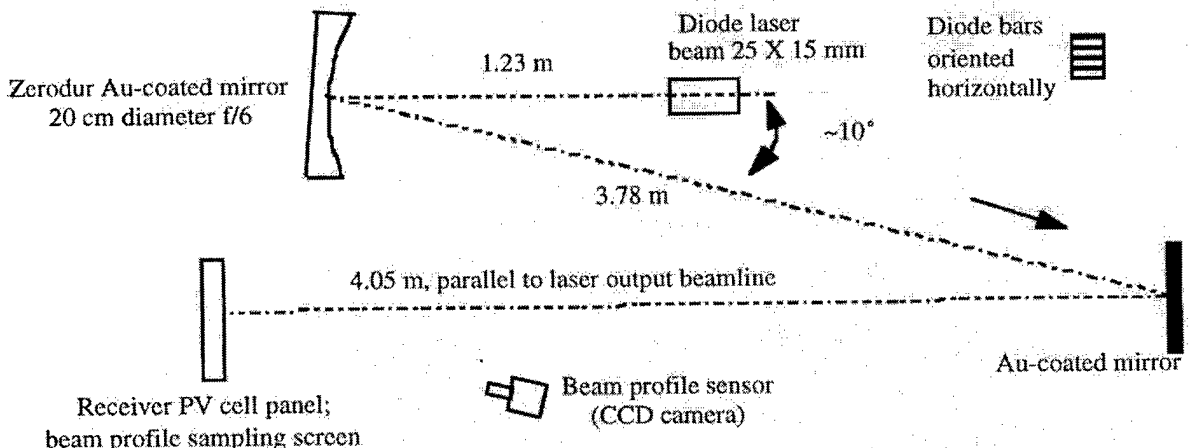

FIGURE 3. Optical layout, viewed from above.

location is shown in Figure 5. It was anticipated that directly reimaging the diode array on the receiver would give a nonuniform flux at the receiver, since the array surface is not uniformly bright, but that a comparatively small defocusing would blur the stripe pattern and yield a uniform spot. The degree of defocusing available with this small source and short range was not large, however. Also, the uniformity of the diode bars was poor, especially at the near-threshold operating conditions, creating large-scale variations in output across the transmitter surface.

However, the high peak power observed in one section of the output pattern was entirely unexpected. We believe this was due to misalignment of the microlens on one diode bar, with the result that its output was directed about 2 beamwidths away from the nominal beam direction. With the particular ranges and optics used, this would cause both a dip in flux at the receiver where that bar should have illuminated, and a peak where two bar outputs overlapped.

Due to the nonuniformity, operating the transmitter at even ~20 watts resulted in localized hot spots at the receiver. Changes in the surface appearance of the receiver during operation suggested that the plastic cover and/or the low-temperature solder interconnections were approaching melting. Post-experiment examination of the receiver revealed a crack in one cell. Operation with a larger receiver area (a ~1 m^2 PV cell panel) and higher power was planned but not completed.

Power Received

Despite these problems, the 3-cell string was placed under the peak of the beam pattern with the laser operating at 42 V, 20 A. The output of the 3-cell string was measured at:

Voc (open circuit voltage): 1.93 V (average; fell from 1.99 to 1.85 volts as the receiver was heated by the beam)

Isc (short circuit current): 1.19A

Assuming a power factor (ratio of Voc * Isc to power into a matched load) of 85%, the power extractable by a matched load would have been 1.8 W. Due to the nonuniform illumination, the estimated power available from the full 9-cell receiver was between 3.6 and 4.5 watts.

The flux at the receiver, at the pattern peak, was measured with the power meter at 1850 W/m^2, or roughly 1.5 times full solar illumination. Integrating the beam profile over the active cell area, vs. the total integrated beam profile, gave the fraction of the laser power illuminating the cells as 22%. At 28.6 W laser output, and with mirror losses of ~10%, the optical power on the 3-cell string was approximately 5.7 W, giving a cell efficiency of 1.8/5.7 = 32%.

There is some uncertainty about this value, as a similar integration estimates the fraction of the laser power entering the power meter aperture (2.6 cm^2) as 0.0081; this would correspond to total beam power at the receiver of (.185*2.6/0.0081) = 59.5 watts, and thus a laser power of ~65 watts, significantly higher than the 28.6 W previously measured at this laser current. The source of the discrepancy is not known. The corresponding PV cell efficiency if this power estimate is correct is ~14%, which would be surprisingly low.

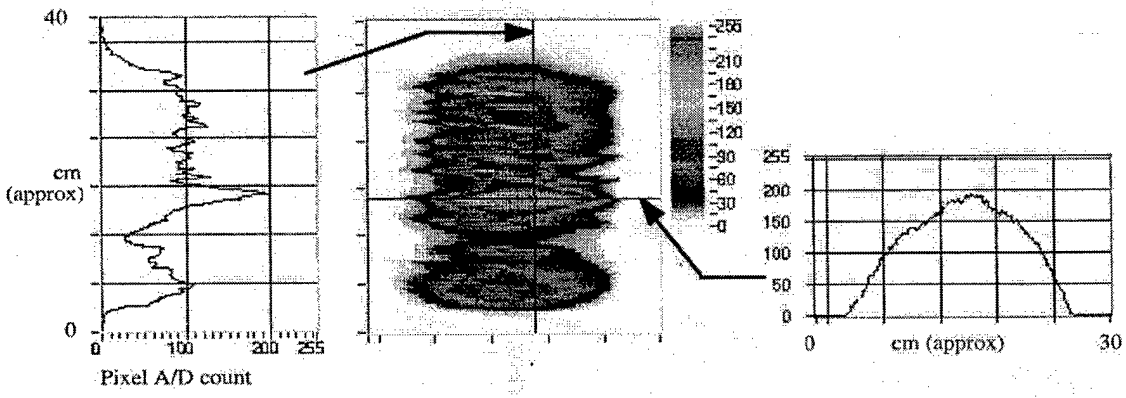

FIGURE 5. Beam profile at receiver.

Fuel Cell/Motor Operation

The receiver was used to directly drive a small (1 W) electric motor with the 3-cell string, and to simultaneously charge a demonstration-sized regenerative fuel cell with the 6-cell string. The fuel cell, operating as an electrolyzer, developed bubbles indicating significant gas production at a laser current between 18 and 20 A.

DISCUSSION

This effort was unfortunately cut short after the first "power transmission". As a result, the overall efficiency and power transmitted were both low and poorly measured. The estimated efficiency and power are shown in Table 1.

However, the required steps to improve this efficiency in the existing experimental setup are clear:

1. Operate at substantially higher transmitter power to improve transmitter efficiency and uniformity.

2. Improve the uniformity of the beam at the receiver. At a minimum, the worst-misaligned diode bar may be blocked off to reduce the severest "hot spot". Some types of "beam scramblers", including the lens ducts used to couple diode array outputs to solid-state laser media, are nearly radiance-preserving, and can be used to generate a more uniform output.

With these two improvements, we would anticipate being able to transmit in excess of 100 watts over ~30 meters, with an end-to-end efficiency of approximately 10%, using a larger (~1/2 meter square) receiver array

A third upgrade would use an anamorphic lens or prism to fill the available focusing reflector aperture, rather than using only a narrow strip. This would extend the usable range to 60 to 100 meters, which would exceed the available laboratory path and require moving the tests outdoors or to a larger facility.

Since the range is linearly proportional to the transmitting aperture, larger optics could significantly extend the useful range. Using a 1 meter aperture (of substantially less than telescope quality), the existing transmitter could send useful power (nominally defined as received flux * PV efficiency > sunlight flux * PV efficiency in sunlight) over approximately 1 km.

There are few fundamental limits to increasing the transmitter fluence substantially. In particular, higher power diode bars with 1- or 2-dimensional microlens arrays can clearly provide one more order of magnitude in fluence in the foreseeable future. Arrays of single-mode diodes, which can be accurately focused on both axes, can potentially provide 10^{-6} steradian divergence from diodes on <1 mm centers; at 1 watt per diode, such arrays could exceed 10^{12} W/m^2-sr.

The problem of uniformity will be automatically reduced in larger systems, because the number of individual diode bars will be greatly increased. In the current system, defocusing the system sufficiently to significantly smooth the received flux also spread the overall beam substantially; this would be much less true in a system with 100 or more individual diode arrays. Alternatively, large systems may use multiple small transmitting apertures, since the received flux is independent of the distribution of the transmitting aperture area; in this case many individual

TABLE 1. Demonstrated and Projected Efficiencies of Noncoherent Power Beaming

	Demonstrated			Projected[a]			Achievable[b]		
	Power, W	Efficiency, %	Cumulative Eff., %	Power, W	Efficiency, %	Cumulative Eff., %	Power, W	Efficiency, %	Cumulative Eff., %
DC power	860		100	1540		100	2000 (nominal)		100
Diode array output	28.6	3.4	3.4	243	16	16	900	45	45
Transmission	25.7	90	3.1	219	90	14.4	810	90	41
Receive area/beam area	5.7	22	0.67	109	50	7.2	650	80	33
Cell efficiency	1.8	32	0.21	35	32	2.3	260	40	13

[a] Using the existing source and PV cells in a follow-on experiment

[b] Using currently-available laser diodes and PV cells

nonuniform patterns would be averaged. However, this will remain a key issue for noncoherent array transmissions, and further analysis and experiments on the effect of such nonuniform illumination on PV cell arrays is needed.

ACKNOWLEDGMENTS

This work was funded by the NASA Marshall Space Flight Center. The authors wish to thank Edward E. Montgomery IV of NASA for his assistance in obtaining support, Scott Mitchell and Blake Myers for their extensive assistance in the conducting these tests, and Camille Bibeau for permission to use the LLNL Laser Program's hardware and facilities for this effort. Work at LLNL is conducted under the auspices of the U.S. Department of Energy, Contract W-7405-Eng-48.

REFERENCES

Beach, R., Mundinger, D., Benett, W., Sperry, V., Comaskey, V., and Solarz, R., "High-Reliability Silicon Microchannel Submount for High Average Power Laser Diode Arrays", *Appl. Phys. Lett.* **56**, pp. 2065-2067 (1990).

Comaskey, B. J., et. al., " High Average Power Diode Pumped Slab Laser", IEEE J. of Quantum Electronics, Vol. 21, No. 4, April 1992, pp. 992-996, cf. p. 993 and Fig. 2.

Landis, G., "Applications for Space Power by Laser Transmission," in *Laser Power Beaming*, edited by J. V. Walker and E. E. Montgomery IV, Los Angeles, SPIE Conference Proceedings Vol. 2121, 1994, pp. 252-255.

Mitchell, S., Lawrence Livermore National Laboratory, personal communication, 1997.

Mitlitsky, F., Colella, N. J., Myers, B., and Anderson, C. J., "Regenerative Fuel Cells For Solar Powered Aircraft," 28th Intersociety Energy Conversion Engineering Conference (IECEC), August 9-13 (1993); UCRL-JC-113485.